

# Spectroscopy, *MOST* Photometry, and Interferometry of MWC 314: Is it an LBV or an interacting binary?

Noel D. Richardson<sup>1\*</sup>, Anthony F. J. Moffat<sup>1</sup>, Raphaël Maltais–Tariant<sup>1</sup>, Herbert Pablo<sup>1</sup>, Douglas R. Gies<sup>2</sup>, Hideyuki Saio<sup>3</sup>, Nicole St-Louis<sup>1</sup>, Gail Schaefer<sup>4</sup>, Anatoly S. Miroshnichenko<sup>5</sup>, Chris Farrington<sup>4</sup>, Emily J. Aldoretta<sup>1</sup>, Étienne Artigau<sup>1</sup>, Tabettha S. Boyajian<sup>6</sup>, Kathryn Gordon<sup>2</sup>, Jeremy Jones<sup>2</sup>, Rachel Matson<sup>2</sup>, Harold A. McAlister<sup>2</sup>, David O’Brien<sup>7</sup>, Deepak Raghavan<sup>2</sup>, Tahina Ramiamananantsoa<sup>1</sup>, Stephen T. Ridgway<sup>8</sup>, Nic Scott<sup>4</sup>, Judit Sturmann<sup>4</sup>, Laszlo Sturmann<sup>4</sup>, Theo ten Brummelaar<sup>4</sup>, Joshua D. Thomas<sup>9</sup>, Nils Turner<sup>4</sup>, Norm Vargas<sup>4</sup>, Sergey Zharikov<sup>10</sup>, Jaymie Matthews<sup>11</sup>, Chris Cameron<sup>12</sup>, David Guenther<sup>13</sup>, Rainer Kuschnig<sup>11,14</sup>, Jason Rowe<sup>15</sup>, Slavek Rucinski<sup>16</sup>, Dimitar Sasselov<sup>17</sup>, and Werner Weiss<sup>14</sup>

<sup>1</sup> *Département de physique and Centre de Recherche en Astrophysique du Québec (CRAQ), Université de Montréal, C.P. 6128, Succ. Centre-Ville, Montréal, Québec, H3C 3J7, Canada*

<sup>2</sup> *Center for High Angular Resolution Astronomy, Department of Physics and Astronomy, Georgia State University, P. O. Box 5060, Atlanta, GA 30302-5060, USA*

<sup>3</sup> *Astronomical Institute, Graduate School of Science, Tohoku University, Sendai, Miyagi 980-8578, Japan*

<sup>4</sup> *The CHARA Array, Mount Wilson Observatory, 91023 Mount Wilson CA, USA*

<sup>5</sup> *Department of Physics and Astronomy, University of North Carolina at Greensboro, Greensboro, NC 27402-6170, USA*

<sup>6</sup> *Yale University, New Haven, CT 06520-8101, USA*

<sup>7</sup> *Max Planck Institute for Radio Astronomy, P.O. Box 20 24, D-53010 Bonn, Germany*

<sup>8</sup> *National Optical Astronomy Observatory, 950 North Cherry Ave., Tucson, AZ 85719, USA*

<sup>9</sup> *Department of Physics, Clarkson University, 8 Clarkson Ave, Potsdam, New York 13699, USA*

<sup>10</sup> *Instituto de Astronomía, Universidad Nacional Autónoma de México, Ensenada, BC 22860, Mexico*

<sup>11</sup> *Department of Physics and Astronomy, University of British Columbia, 6224 Agricultural Road, Vancouver, BC V6T 1Z1, Canada*

<sup>12</sup> *Department of Mathematics, Physics & Geology, Cape Breton University, 1250 Grand Lake Road, Sydney, Nova Scotia B1P 6L2, Canada*

<sup>13</sup> *Institute for Computational Astrophysics, Dept. of Astronomy and Physics, St Mary's University Halifax, NS B3H 3C3, Canada*

<sup>14</sup> *University of Vienna, Institute for Astronomy, Türkenschanzstrasse 17, A-1180 Vienna, Austria*

<sup>15</sup> *NASA Ames Research Center, Moffett Field, CA 94035, USA*

<sup>16</sup> *Dept. of Astronomy and Astrophysics, University of Toronto, 50 St George Street, Toronto, ON M5S 3H4, Canada*

<sup>17</sup> *Harvard-Smithsonian Center for Astrophysics, 60 Garden Street, Cambridge, MA 02138, USA*

arXiv:1510.00324v1 [astro-ph.SR] 1 Oct 2015

**ABSTRACT**

MWC 314 is a bright candidate luminous blue variable that resides in a fairly close binary system, with an orbital period of  $60.753 \pm 0.003$  d. We observed MWC 314 with a combination of optical spectroscopy, broad-band ground- and space-based photometry, as well as with long baseline, near-infrared interferometry. We have revised the single-lined spectroscopic orbit and explored the photometric variability. The orbital light curve displays two minima each orbit that can be partially explained in terms of the tidal distortion of the primary that occurs around the time of periastron. The emission lines in the system are often double-peaked and stationary in their kinematics, indicative of a circumbinary disc. We find that the stellar wind or circumbinary disc is partially resolved in the  $K'$ -band with the longest baselines of the CHARA Array. From this analysis, we provide a simple, qualitative model in an attempt to explain the observations. From the assumption of Roche Lobe overflow and tidal synchronisation at periastron, we estimate the component masses to be  $M_1 \approx 5M_\odot$  and  $M_2 \approx 15M_\odot$ , which indicates a mass of the LBV that is extremely low. In addition to the orbital modulation, we discovered two pulsational modes with the *MOST* satellite. These modes are easily supported by a low-mass hydrogen-poor star, but cannot be easily supported by a star with the parameters of an LBV. The combination of these results provides evidence that the primary star was likely never a normal LBV, but rather is the product of binary interactions. As such, this system presents opportunities for studying mass-transfer and binary evolution with many observational techniques.

**Key words:** stars: early-type – binaries: close – stars: individual (MWC 314) – stars: winds, outflows – stars: mass loss – stars: variables: S Doradus

**1 INTRODUCTION**

Massive stars provide much of the energy input in the Universe. Their high mass-loss rates and supernova explosions provide important feedback to the star formation processes and total energy input of galaxies. Recent advances in stellar modelling (e.g., Groh et al. 2013) show that the supernova progenitors for core collapse supernovae come in many different types that include red supergiants (RSG), blue supergiants (BSG), Wolf-Rayet (WR) stars, and Luminous Blue Variables (LBVs).

Massive stars tend to be found primarily in binary systems. The O stars are thought to have a bound companion about 75% of the time, with most of the exceptions being runaway stars (e.g. Mason et al. 2009). Mason et al. found that O stars in clusters and associations have companions at least 60-80% of the time. Their sample focused on high angular resolution techniques, but also incorporated spectroscopic results. Sana et al. (2012) showed that 71% of O stars will have a binary interaction during their lives. They found that only 29% of the O stars are effectively single (either very-long period binary stars or actually single), meaning that evolutionary models that do not incorporate binary effects will have limited applicability.

LBVs are among the most unusual classes of massive stars. They have attained a highly luminous, unstable state that shows remarkable mass-loss and variability. The normal mass-loss rates range between  $10^{-6} - 10^{-3} M_\odot \text{ yr}^{-1}$ , which has typically led to the conclusion that these objects are post-main sequence, hydrogen-shell-burning massive stars that represent the transitional phase between the

main sequence O stars and the helium-burning WR stars (e.g. Humphreys & Davidson 1994; van Genderen 2001). However, the recent analysis by Groh et al. (2013) shows that lower initial mass stars (20–25  $M_\odot$ ) can become LBVs after the RSG phase, and then explode as type II supernovae during the final LBV phase.

With a large binary fraction for the main-sequence O stars, one may also expect to see a high binary fraction in the post-main sequence massive stars. However, the binary fraction for WR stars is low (40%) as noted by Vanbeveren & Conti (1980). An examination of the multiplicity and binarity of LBVs was reported by Martayan et al. (2012) who reported a remarkably low binary fraction of only 11%. There are only four well-studied LBV binary systems:  $\eta$  Carinae (e.g. Richardson et al. 2010, Madura et al. 2013 and references therein), MWC 314 (Lobel et al. 2013, hereafter L13), HD 5980 (e.g. Koenigsberger et al. 2010), and R 81 (HDE 269128; Tubbesing et al. 2002).  $\eta$  Car is by far the most studied of all these binary systems, but analyses of both  $\eta$  Car and the other systems have not produced reliable, model-independent masses yet. For example, in the R 81 system, a clear eclipse is seen in the light curve while the primary is in front of the secondary in our line of sight, but the secondary eclipse is small, and similar in amplitude to the pulsations in the system. The masses of both stars are only known to a factor of  $\sim 2$ , which does not provide much insight into the masses of these evolved massive stars (Tubbesing et al. 2002). HD 5980 shows orbital variations due to both colliding winds and binarity, and the system shows long-term evolution in its light curve similar to that of other LBVs (Koenigsberger et al. 2010), but the spectrum reveals that the two stars both appear as WNh stars (Wolf-Rayet stars showing nitrogen-enrichment and hydrogen). This makes the

\* E-mail: richardson@astro.umontreal.ca

temperature of HD 5980 hotter than all other LBVs so a determination of its mass may not be typical of LBVs. MWC 314 is unique in that the orbital period is semi-short (60.8 d), it is well-placed in the sky ( $\delta = +14^\circ$ ), and bright enough to allow high resolution studies of the star and its environs with multiple observing techniques.

MWC 314 (BD+14 3887, V1429 Aql, Hen 3-1745) has been examined in a few key studies, which were largely reviewed in the recent work of L13. Miroshnichenko (1996) found the star to be of high luminosity, exhibit a strong interstellar reddening, and to have a similar luminosity to the prototypical LBV, P Cygni. Miroshnichenko et al. (1998) then determined the spectral characteristics and found it to be very similar to P Cygni, with an estimated distance of  $3.0 \pm 0.2$  kpc. Wisniewski et al. (2006) presented a long-term spectropolarimetric and spectroscopic study of MWC 314, finding the first evidence of  $H\alpha$  variability. They found that the polarisation was variable in a way reminiscent of an asymmetric wind. MWC 314 was shown to be a spectroscopic binary by Muratorio et al. (2008), but they underestimated the orbital period. L13 measured absorption lines of S II and Ne I, which are thought to be photospheric, and found the system to have a 60.8 d orbit with a small eccentricity of  $e = 0.23$ . They also demonstrated that the  $V$ -band photometry from the All Sky Automated Survey is modulated on the orbital time scale, and their interpretation of the light curve includes two partial eclipses.

L13 used a model of the single-lined spectroscopic radial velocity orbit and photometric light curve to help estimate the mass ratio and system parameters. They found that the primary star had typical parameters for an LBV, with  $T_{\text{eff}} = 18,000\text{K}$ ,  $\log g = 2.26$ ,  $M \simeq 40M_{\odot}$ , and  $R \simeq 87R_{\odot}$ . The secondary star's parameters were very unusual in that they suggest the companion is a yellow giant. This interpretation is inconsistent from an evolutionary standpoint because the secondary should not be able to reach an advanced evolutionary state (cool temperature) given the short lifetime of the evolved primary star. Liermann et al. (2014) present NIR  $K$ -band spectrophotometry of MWC 314 and some B[e] stars. Several of these stars show CO spectral features that would be consistent with a companion similar to that suggested by L13, but MWC 314 does not show these features.

L13 also developed a three-dimensional wind model to create synthetic He I wind lines for comparative purposes showing some evidence for an asymmetric wind, which was further developed by Lobel et al. (2015). This asymmetric wind has a density enhancement on the leading hemisphere of the LBV that feeds gas into a circumbinary disc. Further, they obtained an image of the  $H\alpha$  emission nebula surrounding the star which shows a bipolar structure on large scales (Marston & McCollum 2008), but appears spherically symmetric at small scales of a few arcseconds.

In this paper, we present a variety of new observations (spectroscopy, photometry, and long-baseline near-infrared interferometry) of the MWC 314 system, which is described in Section 2. In Section 3, a revised single-lined orbit based upon new spectroscopy and the work of L13 is presented and discussed. Section 4 discusses the orbital light-curve, as well as the discovery of pulsational modes. Our interferometric results are presented in Section 5. In Section 6, we present a general discussion of the system with respect to

the fundamental parameters, pulsations, and the interferometric results. We conclude our study in Section 7.

## 2 OBSERVATIONS

### 2.1 Spectroscopy

We observed MWC 314 with a variety of telescopes and instruments with the primary goal being to better constrain the single-lined orbit. The telescopes used include the CTIO 1.5 m operated by the SMARTS Consortium, the Observatoire du Mont Mégantic 1.6 m, McDonald Observatory's Struve 2.1 m and Harlan Smith 2.7 m, the Mercator 1.2 m, and the San Pedro Martir 2.1 m telescopes. All observations were reduced using standard techniques for long-slit or echelle spectroscopy utilising bias frames and flat fields with either IRAF<sup>1</sup> or custom software. Wavelength calibration was accomplished through emission-line comparison spectra taken before or after each observation. A spectroscopic observing log is presented in Table A1 that details the telescopes, spectrographs, and data.

L13 measured the absorption lines S II  $\lambda\lambda 5454, 5474, 5647$  and Ne I  $\lambda 6402$ , due to their lack of blending with the large number of emission lines in the spectrum of MWC 314. We sought to include these lines whenever possible. Radial velocity measurements were made through Gaussian fits of the spectral lines. We found that we were able to use the Ne I  $\lambda 6402$  line for all data sets, but the S II lines often suffered from lower S/N and were unreliable. The McDonald Observatory observations provided excellent data for S II  $\lambda 5647$ , but were not usable for the S II  $\lambda\lambda 5454, 5474$  lines. The data from the CTIO 1.5 SMARTS fiber-fed bench-mounted echelle<sup>2</sup> (Barden & Ingerson 1998) were only usable around the Ne I line. However, the data obtained with the CTIO 1.5 m and the CHIRON spectrograph (Tokovinin et al. 2013) have higher S/N across the optical spectrum. The spectroscopic data discussed in L13 were obtained with the Mercator 1.2 m telescope and the HERMES spectrograph (Raskin et al. 2011), which we also used to obtain three additional spectra of comparable quality. The spectrum taken at San Pedro Martir was extremely useful due to the orbital phase observed (most negative radial velocity) and good S/N. The data from the Observatoire du Mont Mégantic (OMM) were of much lower spectral resolution, and we only obtained two spectra that had high enough S/N to measure accurately a radial velocity from the weak absorption lines.

### 2.2 Ground-Based Photometry

Broadband  $BVRI$  photometry was obtained throughout the 2010–2012 calendar years with the American Association of Variable Star Observers automated telescope located

<sup>1</sup> IRAF is distributed by the National Optical Astronomy Observatory, which is operated by the Association of Universities for Research in Astronomy (AURA) under cooperative agreement with the National Science Foundation.

<sup>2</sup> <http://www.ctio.noao.edu/~atokovin/echelle/FECH-overview.html>

at Lowell Observatory. The telescope<sup>3</sup> is a Celestron C11 Schmidt-Cassegrain instrument with an aperture of 28 cm. Imaging was accomplished with an SBIG ST-7XME camera, which yields images with a field of view of  $14 \times 9$  arcmin. The reductions utilise dark, bias, and flat frames, and typically the scattered light background leads to a photometric accuracy of 1–2%. The differential photometry was done relative to another star in the field, HD 231237, which shows a constant light curve in the All Sky Automated Survey (ASAS; Pojmański 2002) and was classified as G5 by Cannon (1925).

We wished to obtain a reasonable magnitude estimate of MWC 314 relative to the comparison star, so magnitudes for the comparison star were obtained from the AAVSO Photometric All-Sky Survey (APASS)<sup>4</sup>, which measured  $B = 11.48 \pm 0.047$ ,  $V = 10.716 \pm 0.027$ ,  $g' = 11.024 \pm 0.032$ ,  $r' = 10.497 \pm 0.016$ , and  $i' = 10.228 \pm 0.054$  for HD 231237. The Johnson  $R$  magnitude was obtained by using the relations given by Kent (1985), which gave  $R = 9.95$ . Similarly, we transformed these data into Johnson  $I$  using the transformations given by Windhorst et al. (1991), which yields  $I = 9.48$ . We present the measurements of MWC 314 calibrated by HD 231237 in Table A4. However, we caution that we did not perform any colour transformations on the data, so the magnitudes may have small systematic errors related to airmass at the time of observation.

### 2.3 Precision Photometry from *MOST*

We observed the system with the micro-satellite *MOST* (*Micr variability and Oscillations of STars*) which has a 15-cm Maksutov telescope with a custom broad-band filter covering 3500–7500 Å. The sun-synchronous polar orbit has a period of 101.4 minutes ( $f = 14.20 \text{ d}^{-1}$ ), which enables uninterrupted observations for up to eight weeks for targets in the continuous viewing zone. A pre-launch summary of the mission is given by Walker et al. (2003). The satellite was never intended to observe a target for several months and recover time-scales on the order of the length of the data.

MWC 314 was observed for a small portion of every spacecraft orbit for 55 d, spanning 2014 June 19 to 2014 August 15 in the direct imaging mode. Our data were taken over short orbital segments, which we then averaged during each 5–10 minute interval to have precise photometry from the orbital means. The photometry was extracted using the standard *MOST* pipeline (Walker et al. 2003), and we show two different versions of the final light-curve in this paper, which are given in Tables A6 and A7. The first uses a trend-removed data that removes the binary-induced signal from the light curve. We also attempted to extract the binary light curve by using a raw extraction that allowed for the signal to remain. It was difficult to recover the binary signal, as a remaining instrumental response needed to be removed through a comparison with all guide stars that were observed simultaneously, and then fitting and removing an average “instrumental” trend from the data. We note that a small portion of this light curve could not be corrected for the instrumental response. The long time-series from *MOST* was not continuous due to data gaps induced from passages

through the South Atlantic Anomaly, problems with scattered light that is more prominent during northern summer months, and communications errors. Nevertheless, the *MOST* observations provide a unique photometric data set to explore the variability of this object.

### 2.4 Long Baseline, Near-Infrared Interferometry

We obtained multiple epochs of long baseline near-infrared interferometry using the CHARA Array and the Classic (ten Brummelaar et al. 2005) and CLIMB beam combiners (ten Brummelaar et al. 2013) in the  $K'$ -band during the calendar years 2010–2013. The CHARA Array is a  $\gamma$ -shaped interferometric array of six 1-m telescopes with baselines ranging from 34 to 331 meters in length. Our observations were primarily at longer baselines, but we obtained a few measurements with short baselines. The nights of observations, baselines used, and calibrators for each observation are listed in Table A2.

To measure the instrument response and calibrate our data, we observed calibrator stars with small angular diameters both before and after each observation of MWC 314. Namely, we observed the calibrator stars HD 174897 ( $\theta_{LD} = 0.652 \pm 0.038$  mas; Boyajian et al. 2012), HD 182101 ( $\theta_{LD} = 0.367 \pm 0.017$  mas; Berger et al. 2006, Baines et al. 2010), and HD 184606 ( $\theta_{LD} = 0.236 \pm 0.050$  mas; van Belle et al. 2008). These calibrators have diameters known from fits to the spectral energy distribution and have all been reliable for previous interferometric studies. The data were reduced using the standard CHARA reduction pipeline (ten Brummelaar et al. 2005, 2013). The visibilities and closure phases were averaged over each observing block. The calibrated OIFITS data files (Pauls et al. 2005) will be available through the JMMC archive<sup>5</sup> or upon request, but we also include tabulated visibilities in Table A5.

Schaefer et al. (2014) describe the effects of emission lines on the errors and measurements of  $V^2$ . An emission line reduces the effective bandpass over which the fringe amplitude is measured causing the true visibility to be smaller than if a fixed bandpass was assumed. We measured the effective bandpass through comparisons of the width of the power spectra of both calibrator stars and MWC 314, and found that this is typically an effect of  $< 3\%$ , much smaller than the typical error of our measurements. Further, we compared a  $K'$ -band filter response with a single NIR spectrum of MWC 314 we obtained with the Mimir instrument and the Lowell Observatory 1.8 m telescope (Clemens et al. 2007). This spectrum was reduced with the standard Mimir pipeline<sup>6</sup> and flux-calibrated and telluric-corrected using the `xtellcor` package (Vacca et al. 2003). This spectrum was then convolved with the filter response, and we found that the effective width was within 1–2% of the nominal width. These values show that there was little change in the visibilities, but the resulting uncertainty in the width of the filter ( $\sim 3\%$ ) was added in quadrature to the pipeline-produced error.

<sup>3</sup> <http://www.aavso.org/w28>

<sup>4</sup> <http://www.aavso.org/apass>

<sup>5</sup> <http://www.jmmc.fr/oidb.htm>

<sup>6</sup> <http://people.bu.edu/clemens/mimir/software.html>

### 3 THE SINGLE-LINED SPECTROSCOPIC ORBIT

The optical spectrum of MWC 314 consists of four different kinds of spectral lines, which are illustrated in the spectral atlas of Miroschnichenko et al. (1998). First, there are absorption lines, such as those measured by L13. These are thought to be photospheric in origin, with minimal contamination by the wind. These lines are similar to the photospheric metal lines observed in the B7 Ia supergiant HD 183143 (Chentsov et al. 2003), but are typical of any early- or mid-B supergiant. Secondly, the wind of the system is best seen in the strong Balmer lines and He I emission lines. The Balmer lines do not show a P Cygni absorption component, but the He I lines have P Cygni absorption that shows orbitally-modulated variability where the absorption strengthens at certain orbital epochs (L13). Thirdly, there are many lines of singly-ionised metals, such as Fe II, that show double-peaked emission profiles. These lines were shown by L13 to be constant in radial velocity and are thought to originate from a circumbinary disc. In reality, some of the double-peaked emission lines and Balmer lines are likely formed in a combination of the circumbinary disc and stellar wind. The fourth and final type of lines are the interstellar absorption lines. These lines are very complicated, often showing several absorption components due to the extreme extinction of MWC 314 ( $A_V = 5.7$ ; Miroschnichenko 1996).

We measured radial velocities through Gaussian fits of the same absorption lines as measured by L13 to refine the spectroscopic orbit of MWC 314. The lines used were discussed in Section 2.1, and the new radial velocities are presented in Table A3. We estimate the errors on most of the data points to be on the order of  $\pm 2 \text{ km s}^{-1}$ , and a little better ( $\pm 1 \text{ km s}^{-1}$ ) for the HERMES spectra. The data are shown in Figure 1 with our orbital elements presented in Table 1. The data span the calendar years 2001–2013, so we derived the orbital period through a time-series analysis of these new radial velocities combined with the velocities reported by both Muratorio et al. (2008) and L13. We confirm the orbital period, although we adopt a more conservative error than reported by L13. Note that L13 set phase zero at inferior conjunction of the visible star and also measure  $\omega$  from this epoch, instead of the standard spectroscopic method of setting  $\omega$  equal to the angle between the ascending node and periastron. The values of  $T$  and  $\omega$  given in Table 1 for the L13 solution are referenced to periastron in the standard way. The errors reported by L13 are generally smaller than ours, however, the PHOEBE code they used does not directly estimate the errors of the parameters, so we suspect that these are underestimated. We show orbital parameters in Table 1 for L13’s fit, our fit to their data showing more realistic errors, an independent fit to only our new data, and a combined fit to all data available from Muratorio et al. (2008), L13, and our new data. All the solutions are comparable, and we adopt the combined fit for the remainder of this analysis.

The orbit is well-behaved with a moderate eccentricity ( $e = 0.29$ ). The measured value of  $\omega$  is such that the primary is in front of the secondary at phase 0.098, and the secondary is in front of the primary at phase 0.760. We find that the mass function,  $f(M)$  is somewhat large, with a value of  $4.0 \pm 0.3 M_\odot$ .

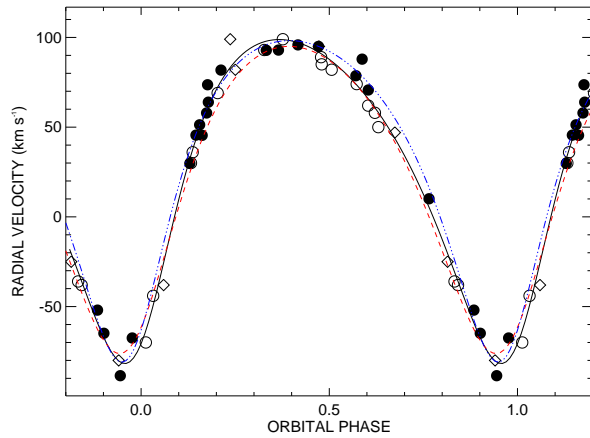


**Figure 1.** The revised single-lined spectroscopic orbit with data sources marked. Phase 0 indicates the periastron passage. New data are shown as solid points, the open circles are from L13, and the open diamonds are from Muratorio et al. (2008). The black line represents the combined fit of all data, while the blue dash-dotted line is the fit from only our measurements, and the red dashed line is the solution from L13.

### 4 THE PHOTOMETRIC VARIATIONS

In Figure 2, we show the  $V$ -band photometry from the AAVSO.net telescope (open circles) and the *MOST* satellite (solid points) phased to the periastron and orbital period found with the spectroscopic orbit. We removed the pulsational signature from the *MOST* data for this plot (see Section 4.2). We performed time-series analysis of the ground-based data and found that the period ( $P = 60.5 \pm 2.0$ ) we derive from a Lomb-Scargle periodogram (Scargle 1982) was consistent with that of the spectroscopy, so we adopt the spectroscopic period due to the longer duration of the spectroscopic observations and smaller error in the period determination. The larger scatter in Figure 2 results from the 1–2% measurement errors inherent to the observations, the pulsational variations still present in the AAVSO data, and from possible long-term variability of the system (e.g. L13). We note that the light curve resembles the variations presented by L13, who used PHOEBE to model the variations as tidally induced variability with partial eclipses.

#### 4.1 Ellipsoidal Variations

The photometric variability is likely induced by the star being distorted gravitationally by the companion. This kind of variability has been known and calculated for many years (e.g. Beech 1985) and is referred to as ellipsoidal variability. In recent years, the modeling of eclipsing binaries has been greatly enhanced by the code PHOEBE (PHysics Of Eclipsing BinariEs; Prša & Zwitter 2005). This code gives us the freedom to treat this system in a variety of different ways, which we explored to examine the photometric variability. The different models we tested are tabulated in Table 2.

We began fitting the system through a recreation of the model of L13. We used our newly derived radial velocity orbit in Section 3 to set  $T$ ,  $P$ ,  $e$ , and  $\omega$ , leaving us with masses, radii, temperatures, and the orbital inclination as free parameters. The first model (Model #1 in Ta-

**Table 1.** Orbital Elements

Element	units	L13	Our Fit to L13	New data	Combined analysis
$P$	days	$60.799977 \pm 0.000014$	$60.799977$ (fixed)	$60.729 \pm 0.028$	$60.753 \pm 0.003$
$e$		$0.235 \pm 0.003$	$0.28 \pm 0.02$	$0.32 \pm 0.03$	$0.29 \pm 0.01$
$\gamma$	$\text{km s}^{-1}$	$28.4 \pm 0.2$	$27.7 \pm 1.0$	$35.9 \pm 1.8$	$31.2 \pm 0.8$
$K_1$	$\text{km s}^{-1}$	85.6	$90.3 \pm 2.0$	$89.6 \pm 2.4$	$90.3 \pm 1.2$
$\omega$	$^\circ$	$199 \pm 1$	$206.4 \pm 4.0$	$195.1 \pm 6.3$	$208.6 \pm 0.8$
$T$	HJD	$2454951.80 \pm 0.56$	$2454949.75 \pm 0.60$	$2456467.15 \pm 1.02$	$2455618.88 \pm 0.13$
$f(M)$	$M_\odot$	3.63	$4.1 \pm 0.29$	$3.9 \pm 0.3$	$4.0 \pm 0.3$
$a_1 \sin i$	AU	0.465	$0.484 \pm 0.011$	$0.475 \pm 0.014$	$0.479 \pm 0.010$
$N_{\text{observations}}$		16	16	20	43
$r.m.s.$	$\text{km s}^{-1}$	...	3.70	7.20	6.98

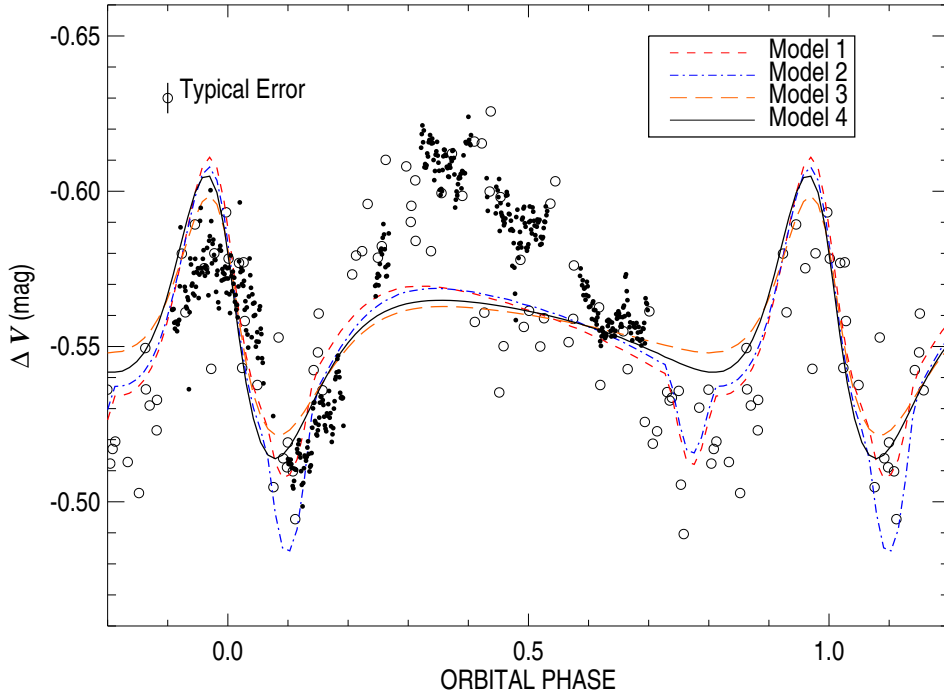


**Figure 2.**  $V$ -band photometry of MWC 314 as a function of phase. The large open points represent our ground-based data. The solid points are orbital means from *MOST* with the pulsational behaviour subtracted off (see Section 4.2). Our reductions could not remove the instrumental artifacts that were at the end of the observing run at phases 0.7–0.85, so those points are omitted. As the instrumental effects could not be eliminated, we did not use these points in our ellipsoidal fit of the photometry. We overplot our best models of the light curve. The dashed lines represent our best understanding of the ellipsoidal variability for the system (Section 4.1), and correspond to models in Table 2.

**Table 2.** PHOEBE Parameters

Element	units	Model #1	Model #2	Model #3	Model#4
$M_p$	$M_\odot$	39.7	39.7	61.1	4.1
$R_p$	$R_\odot$	81.5	81.5	94.1	35.0
$T_{\text{eff},p}$	K	18,000	18,000	18,000	18,000
$M_s$	$M_\odot$	26.2	26.2	40.3	11.3
$R_s$	$R_\odot$	20.6	20.6	23.7	16.4
$T_{\text{eff},s}$	K	6,227	12,000	30,000	25,000
$i$	$^\circ$	73	73	60	60

ble 2) shows ellipsoidal variability and a partial secondary eclipse. This model, along with our other PHOEBE models, suffers from inadequate flux at phases 0.2–0.5, and is overestimated from phases 0.7–0.8. However, the variability near periastron is of a correct amplitude and shape to reproduce the light curve at those phases.

We then adjusted the effective temperature of the secondary (Model #2) to have a hotter secondary star. This demonstrates that the primary is the main source of variation in these models, but the primary eclipse depth is increased drastically. With a small change of the inclination (Model #3), we then found that the eclipses are no longer seen, which is supported by the light curve shape, even if the models do not fully represent the photometry. Further, in Model #3, we increased the temperature to that of an O dwarf in order to have a more realistic companion star.

Lastly, we attempted a low mass solution (Model #4) in which the primary has lost mass via Roche lobe overflow onto the secondary (see Section 6.1). These parameters include a primary with a smaller radius than Models #1–3 and a secondary mass almost three times larger than the primary. With a moderate inclination of  $60^\circ$ , we obtain a model light curve with the same basic shape and amplitude. This shows that the mass ratio derived by L13 can only be considered one possible solution, as the light curve can be reproduced with extraordinary changes in the masses and temperatures, and is not dependent on which star is the more massive component.

For these models, we assumed a semi-detached system where the primary fills its Roche lobe at periastron, as any other configuration provided worse fits of the data. In such a system, we see less flux as we look down the orbital axis (phases 0.76 and 0.10) and observe the strongest flux at quadrature phases (0.96 and 0.37) as we view the small and large profiles, respectively, of the distorted star. Tides in the system attain a maximum near periastron, and yield a more extreme maximum and minimum flux than, as observed. Some problems with the PHOEBE results are likely related to the eccentricity of the system. With eccentric binaries, we have differing values of the separation and Roche potentials as a function of phase. This can lead to changes in the state of the binary from detached to semi-detached over the course of an orbit. The physics involved in such a situation is much more complex and detailed models of such binaries are not yet developed. However, the timing of the primary eclipse is well sampled with *MOST*, and we find no strong evidence of an eclipse event, at least not to the extent of the model presented by L13.

#### 4.2 Pulsational Behavior Discovered with *MOST*

Our photometry from *MOST* (also overplotted in Fig. 2) offers the most precise photometric time-series of the system ever obtained. Unfortunately, *MOST* was never intended to reliably extract astrophysical trends on long time-scales, so the binary-induced signal is not reliable. This is seen to be especially true when we de-trended our data using the light curves of several guide stars in the field, and the *MOST* light curve has a spike at phases  $\phi \sim 0.7 - 0.8$ . However, when the long-timescale trends are removed from the *MOST* light curve, we immediately see evidence of pulsational behaviour in the star. An analysis of these de-trended data with Pe-

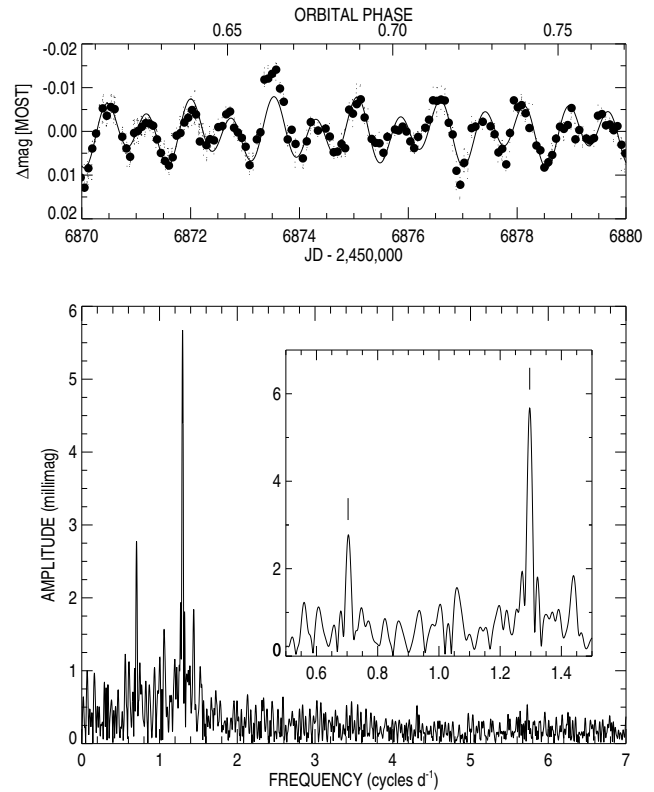


**Figure 3.** A portion of the detrended *MOST* photometry of MWC 314 as a function of time and phase is shown in the top panel. Orbital means are shown as large black points, with each individual measurement shown as a small point. Our two-frequency fit is shown as a solid line in this plot. In the bottom panel, we show the Fourier Transform calculated with Period04, with a zoom on the two frequencies found in the inset panel. The full *MOST* light curve is shown in Fig. A2.

riod04 (Lenz & Breger 2005; Fig. 3) found two significant frequencies, which are listed in Table 3. Each period is represented by a sine wave of the form

$$A \sin(2\pi f \times t + \phi),$$

where  $A$  is the amplitude of the variation in millimagnitudes,  $f$  is the frequency in units of  $\text{day}^{-1}$ ,  $t$  is the time in observed julian day, and  $\phi$  is an offset term in radians that allows for differing the peak time of the sinusoidal wave. These fits explain the data with residuals smaller than one millimagnitude for most data points, which is reasonably consistent with the instrumental performance.

These periods are remarkably short for an LBV, where results of other stars have revealed periods of order several days (see, e.g. van Genderen 2001). However, the blue supergiant HD 163899 (B2Ib/II) was studied by Saio et al. (2006) who found periods of similar duration to MWC 314. L13 have parameters for MWC 314 that indicate a radius of the primary star to be  $\sim 80R_\odot$ , but the blue supergiant with similar periods (HD 163899) has a radius  $\sim 16R_\odot$ . We will further discuss this later in the paper, but the derived radius

**Table 3.** Frequencies found with *MOST*.

Frequency	$A$ (mmag)	$f$ (cycles $\text{d}^{-1}$ )	$\phi$ (radians)	$P$ (d)
1	$5.59 \pm 0.22$	$1.2964 \pm 0.0004$	$0.3847 \pm 0.0063$	$0.7713 \pm 0.0003$
2	$2.61 \pm 0.22$	$0.7032 \pm 0.0008$	$0.6940 \pm 0.0135$	$1.4221 \pm 0.0016$

by L13 is likely much too large to support such short-period pulsations in MWC 314.

## 5 INTERFEROMETRIC RESULTS

The distance of MWC 314 was derived by Miroshnichenko et al. (1998) to be  $3.0 \pm 0.2$  kpc using a radial velocity of  $+55 \text{ km s}^{-1}$  and the kinematical model of Galactic rotation by Dubath et al. (1988). We can now adjust this distance by using the  $\gamma$  velocity of the single-lined orbit we derived in Section 3 ( $\gamma = 31 \pm 1 \text{ km s}^{-1}$ ). From this derived velocity, we find a closer distance to the system of only  $2.4 \pm 0.1$  kpc. We then derive a luminosity from the expected  $V$  magnitude of 9.9, the effective temperature of 18,000 K (e.g. Miroshnichenko et al. 1998, L13), a reddening of  $A_V = 5.7$  mag (Miroshnichenko 1996), and a bolometric correction of  $-1.7$ . The luminosity then becomes  $\log(L/L_\odot) = 5.7$ , with  $M_V = -7.8$  and  $M_{\text{BOL}} = -9.5$ , neglecting any effect of the companion and circumstellar and circumbinary material. This result agrees with that of L13, and indicates that MWC 314 is a near twin of the early B-type hypergiant and prototypical LBV, P Cygni, especially with a derived radius of  $73R_\odot$ . We caution that if the absorption lines used for the orbit form in the outflow, then the  $\gamma$  velocity could be blue-shifted in our line of sight, and this would change this distance estimate.

Our consideration of the CHARA Array results begins with estimates for the angular size of the visible star and binary orbit. We estimated stellar angular diameter by comparing the observed flux distribution  $f_\lambda$  with that for a model photosphere  $F_\lambda$ ,

$$\frac{f_\lambda}{F_\lambda} = \left(\frac{R_\star}{d}\right)^2 10^{-0.4A_\lambda} = \frac{1}{4}\theta_{LD}^2 10^{-0.4A_\lambda}$$

where  $\theta_{LD}$  is the limb darkening angular diameter and  $A_\lambda$  is the wavelength dependent extinction. We made this comparison in the ultraviolet and optical parts of the spectrum where the observed flux is probably dominated by the contribution from the visible star. We followed the example of Miroshnichenko (1996) who used UV spectra from the *International Ultraviolet Explorer* archive and optical magnitudes to set the observed flux estimates. We assumed a flux model from the solar abundance grid of R. Kurucz for atmospheric parameters appropriate for the visible star,  $T_{\text{eff}} = 18000 \text{ K}$  and  $\log g = 2.5$ . We used the extinction law from Fitzpatrick (1999) to set the extinction law  $A_\lambda$  as a function of the reddening  $E(B - V)$  and ratio of total-to-selective extinction  $R$ . Then a fit of the observed fluxes with the relation above was made with parameter values of  $E(B - V) = 1.81 \pm 0.02$  mag,  $R = 3.05 \pm 0.05$ , and  $\theta_{LD} = 0.24 \pm 0.02$  mas. The first two parameters agree within uncertainties with the results of Miroshnichenko (1996). In the following analysis we will assume a uniform disc model for the visible star with an equivalent angular size of  $\theta_{UD} = 0.23$  mas, very slightly smaller

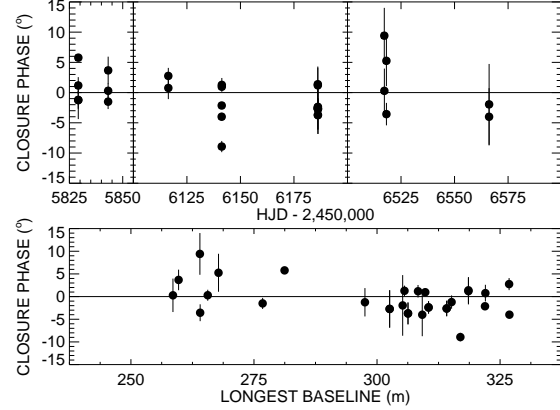


**Figure 4.** Measured closure phases from the CHARA measurements as a function of time (top panel), where each panel represents a different observing period. The bottom panel represents the same measurements as a function of the longest baseline used. The measurements are all very near zero, so we assume that the system is either spherically symmetric or that the circumbinary disc has axial symmetry at the resolution of the observations.

than the limb darkened disc size in the  $K$ -band (Davis et al. 2000). We argue below (Section 6.1) that the angular size of the orbit is also quite small ( $\approx 0.5$  mas) and that the companion may be faint because it is hidden in an obscuring gas torus. Consequently, in this section we will make the simplifying approximation that the entire binary system may be represented by a uniform disc of a size below the resolution limit of our observations.

We collected a large number of squared visibility measurements  $V^2$  with varying baselines (45 – 321 m) that are well sampled on the  $(u, v)$  plane (Fig. A1). Before we attempted to model the visibilities, we examined observations that were obtained with the CLIMB beam combiner, which also gave estimates of the closure phase. These measurements give an indication of the degree of non-axial asymmetry in the data. All measured triple products have values close to zero, as shown in Figure 4. With the small values of the closure phase, we can assume that the light distribution shows an axial symmetry within our errors at the resolution probed with these interferometric observations.

Our adopted interferometric model incorporates the central binary as a uniform disc that is surrounded by a circumbinary disc that is modelled by an elliptical Gaussian on the sky. Any visibility modulation from the binary should be within the errors of the measurements given the small semi-major axis on the sky and the probable faintness of the secondary with respect to the primary. Our model, based upon the methods of Schaefer et al. (2010) and Touhami et al. (2013) has six different fitting parameters, and we have 107 measurements of  $V^2$ . The parameters include the size



of the central source modeled as a uniform disc (UD), the flux from the central source (UD Flux), the flux from the circumbinary disc ( $1 - \text{UD Flux}$ ), the full width at half maximum (FWHM) of the major axis, the FWHM of the minor axis, and the position angle of the major axis of the circumbinary disc on the sky. From the measurement of the major and minor axes, we can compute a disc normal inclination angle from the thin disc approximation. We tabulate the results of various fits in Table 4. We also note that the additional source of error from the correction from the emission line contamination on the interferometry lowered the reduced  $\chi^2$  of these models due to the slightly larger measurement errors in the data.

Model #0 in Table 4 is for a spherically symmetric outflow. The derived uniform disc diameter (UD) for the star is highly unconstrained, but the resulting  $\chi^2$  indicates that the model is on the right track. We explored alternate geometries with an elongated wind or circumbinary disc structure. Model #1 allows all parameters to vary and we derive a nearly edge-on disc with a disc normal inclination that is somewhat larger (but equal within uncertainties) than the the orbital inclination derived from the light curve in Section 4.1.

The next model (#2) fixed the size of the central source to be that of the photospheric size of the primary star as derived from the spectral energy distribution. This is a reasonable choice if we assume little flux emergent from the secondary star. We note that  $\chi^2_{\text{red}}$  is statistically indistinguishable from the models #0 and #1. Lastly, we explored a case where we fixed the central source size, but fit the shell as spherically symmetric (Model #3).

It is also possible that we are not actually resolving a circumbinary shell or disk, but rather the binary itself. We explored the possibility that we were actually resolving the binary by an examination of the densest observation set obtained on 2012 August 01 (HJD 2,456,141), where we obtained 5 measures of the closure phase, and 15 measures of  $V^2$  with CLIMB. We established a grid-based  $\chi^2$  minimization where we calculate a  $\chi^2$  statistic for a large grid of separations in right ascension, declination, and a flux ratio between the two stars. On this night, our best fit was with a separation of 0.697 mas, a position angle of  $263^\circ$ , with a flux ratio between the two stars of 0.997. The reduced  $\chi^2$  statistic was 22.3, meaning our model did not reproduce well the observations. Similar results were seen for the night of 2012 September 16. These “fits” actually provide a  $\chi^2$  statistic much worse than that of a circumbinary shell or disk. We further note that a flux ratio near unity shows that the resolved companion contributes similar levels of flux as the primary, and that the putative separation is on the same order as the resolving limit of the CHARA Array in the  $K'$  band. This flux would likely imply that the orbit would be easily seen to be a double-lined binary, making this result more unlikely.

All of the best  $V^2$  models show that we are resolving a circumbinary shell, but it is unclear if the shell is elongated or spherical. In fact, the models we explored cannot distinguish between them, as all the  $\chi^2$  values are similar. Further, it may be that our errors in the measurements of  $V^2$  are underestimated, making these fits reasonable for these data. The spherical model with a fixed UD is shown in Fig. 5, where we compare the measured and calculated visibilities.

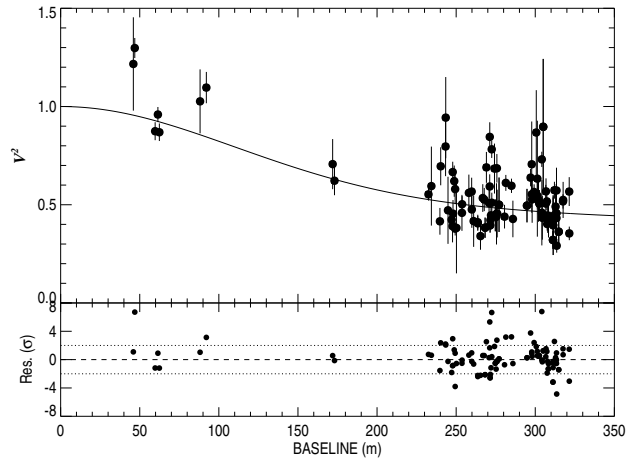


**Figure 5.**  $V^2$  Measurements from the CHARA measurements. We overplot the theoretical visibility curves for the visibility from the spherically symmetric model #3. Most points fall within  $2\sigma$  of this curve, which is shown in the bottom panel.

In this figure, we compare the residuals in the bottom panel by calculating the  $(O - C)$  divided by the measurement error,  $\sigma_{V^2}$ . This shows that the model is reproducing the data within  $\sim 2\sigma$  for most data points. As this model seems to adequately fit the  $V^2$  measurements, we adopt this for the remainder of the analysis. However, we suspect that better data collected in the future may resolve a multi-component model that includes the central star(s) with the stellar wind and the circumstellar disk seen in spectroscopy.

## 6 DISCUSSION

This study has amassed a large dataset that utilised several observing techniques including spectroscopy, photometry, and interferometry. The most exciting results relate to the fundamental parameters of the system, the precision photometry obtained with *MOST* which allowed us to identify pulsational modes in this system, and the exploratory interferometry.

### 6.1 Fundamental Parameters

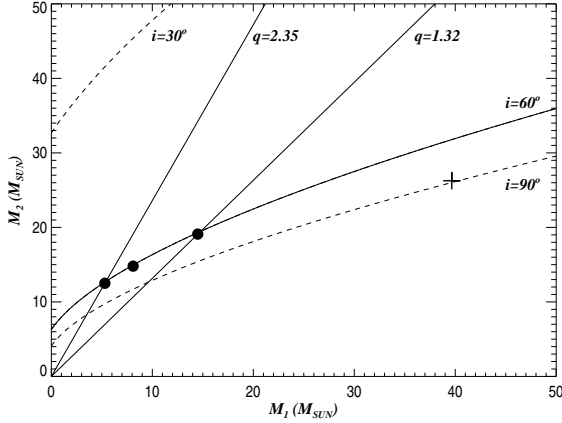
Even though the spectroscopic orbit only shows evidence of the primary star, we are able to determine the mass function and mass sum as

$$M_1 + M_2 = (4.0 \pm 0.3)M_\odot \left(1 + \frac{1}{q}\right)^3 \sin^{-3} i,$$

where  $q = M_2/M_1$  and subscripts 1 and 2 denote the primary (visible) star and secondary star, respectively. The mass relation is shown in Figure 6 where we plot  $M_2$  as a function of  $M_1$  from this equation for three different values of the inclination ( $i = 30^\circ, 60^\circ, \text{ and } 90^\circ$ ). We showed in Section 4.1 that partial eclipses would appear in the orbital light curve for  $i > 70^\circ$  that are not observed. Furthermore, we assumed the maximal tidal distortion possible by setting the radius so large that the star fills the Roche surface at periastron, and consequently any lower inclination would yield a model with a light curve amplitude that was too small, because the size of the tidal modulation varies approximately

**Table 4.** Derived Interferometry Model Parameters. If no error is given, the parameter was held constant.

Model	UD (mas)	UD Flux	Major FWHM (mas)	Minor FWHM (mas)	Position Angle ( $^{\circ}$ )	$i$ ( $^{\circ}$ )	$\chi_{\text{red}}^2$
0	$0.08 \pm 0.88$	$0.67 \pm 0.03$	$1.33 \pm 0.24$	$1.33 \pm 0.24$	...	...	4.24
1	$0.49 \pm 0.14$	$0.76 \pm 0.05$	$2.69 \pm 0.75$	$0.45 \pm 0.51$	$141.9 \pm 4.2$	$80.4_{-20.0}^{+9.6}$	3.89
2	0.23	$0.70 \pm 0.03$	$1.63 \pm 0.49$	$1.23 \pm 0.22$	$114.7 \pm 28.0$	$61.5 \pm 20.0$	4.15
3	0.23	$0.69 \pm 0.02$	$1.37 \pm 0.27$	$1.37 \pm 0.27$	...	...	4.25

**Figure 6.** Masses as a function of inclination and mass ratio. The solid black curve represents the mass function at  $i = 60^{\circ}$ . The dashed lines represent  $i = 30^{\circ}$  (top) and  $i = 90^{\circ}$  (bottom). L13 reported the values shown by a plus sign. We overplot lines for several assumed mass ratios (from Table 5), and filled circles show the corresponding masses for  $i = 60^{\circ}$ .

as  $\sin i$ . Consequently, we suggest that the orbital inclination probably falls within the range from  $i = 50^{\circ}$  to  $i = 75^{\circ}$ .

Sepinsky et al. (2007a, 2009) have investigated how mass transfer eccentric orbit binaries can alter the orbital elements. They show that momentum transfer caused by RLOF can have a large influence on the orbit. In particular, Sepinsky et al. (2007a) show that if the mass ratio reversal has occurred and the mass transfer rate is high, then the eccentricity can increase with time. Their Figure 3 shows that if  $M_1/M_2 < 0.76$  ( $M_1$  is the mass donor = the primary in MWC 314), then continued RLOF will yield a positive time derivative of eccentricity. Thus, if we accept this result, then the fact that we find  $e = 0.29$  in MWC 314 must mean that mass transfer has proceeded beyond mass ratio reversal and that the current mass ratio obeys this limit, so that  $q \geq 1/0.76 = 1.32$ . We show this limit in a solid line on Fig. 6, so that any mass solution must fall to the left of this line diagram.

We argued in Section 4.1 that the tidal modulation of the light curve is best fit if we assume that the visible star fills its Roche lobe at periastron. Because the tides are strongest at periastron, we might also assume that the spin of the star becomes synchronized with the instantaneous orbital rate at that instant. We may use these assumptions to explore the consequences of the Roche geometry for the binary mass ratio. We can estimate the mass ratio by comparing the projected rotational velocity,  $v \sin i$ , to the orbital semi amplitude,  $K_1$  in the manner of Gies & Bolton (1986)

with the expression

$$\frac{v \sin i}{K_1} = \rho \Omega \left(1 + \frac{1}{q}\right) (1 - e^2)^{1/2} \Phi$$

where  $q = M_2/M_1$ . This expression relates the size of the visible star to the Roche radius  $\Phi = \Phi(q)$  (Eggleton 1983) through a fill-out factor  $\rho$  ( $= 1$  for a Roche filling star), and the angular rotational rate is expressed relative to the mean orbital synchronous rate through factor  $\Omega$ . We estimate  $v \sin i$  to be  $\sim 50 \text{ km s}^{-1}$  based upon the FWHM of the absorption profiles seen in our high resolution spectroscopy obtained with high S/N, such as those obtained with the CTIO 1.5 m and CHIRON, consistent with the value reported by L13. Based upon the analysis of the light curve (Section 4.1) and the abundant evidence of mass transfer and mass loss in MWC 314, we assume that the star has a radius that fills its Roche lobe at the periastron passage, so the fill-out factor is given by

$$\rho = (1 - e) = 0.71 \pm 0.02.$$

If the stars are synchronous as the tidal forces peak at periastron passage, then

$$\Omega = \frac{(1 + e)^{1/2}}{(1 - e)^{3/2}}.$$

We evaluated the remaining term for the Roche radius  $\Phi$  above using the general expressions for a star in an eccentric orbit from Sepinsky et al. (2007b). Then we can use the formula above for the observed ratio  $(v \sin i)/K_1$  to find the mass ratio  $q = 2.36$  for the case of spin synchronization at periastron ( $\Omega = 1.90$ ). This mass ratio yields masses of  $M_1 \sim 5.3M_{\odot}$  and  $M_2 = 12.5M_{\odot}$  for intermediate inclination of  $i = 60^{\circ}$ . Note that if some of the line broadening is due to macroturbulence instead of rotational Doppler broadening, then the actual  $v \sin i$  will be smaller than assumed and the resulting mass ratio larger than estimated above. We show the masses derived through this method for both the limiting cases of synchronous rotation at periastron and the eccentricity-growing limit of  $q = 1.32$  in Table 5, along with an intermediate case. All of these solutions are based upon  $i = 60^{\circ}$  and are marked as solid circles in Figure 6. These slower spinning model solutions are particularly relevant, because Sepinsky et al. (2010) find that in some circumstances mass transfer episodes at periastron can result in gas returning back to the donor and decreasing its spin.

We can then calculate the physical radius of the primary star  $R_1$  by multiplying the fractional Roche radius times the fill-out factor and times the semimajor axis. The derived radii are listed in Table 5 using an assumed inclination of  $i = 60^{\circ}$  to find the semimajor axis. We determined the angular diameter of the star in Section 5 from a fit of the spectral energy distribution, and we can use the angular size to relate the physical radius to the distance,  $R/R_{\odot} = 25.7d(\text{kpc})$ .

**Table 5.** Potential Masses of the MWC 314 system<sup>†</sup>, given  $i = 60^\circ$ .

$\Omega$	$q$	$M_1$	$M_2$	$R_1$	d(kpc)	a(AU)	a(mas)
1.90	2.36	5.3	12.5	36.2	1.41	0.79	0.56
1.60	1.82	8.1	14.8	43.0	1.67	0.86	0.51
1.26	1.32	14.5	19.1	54.6	2.12	0.97	0.46

<sup>†</sup> To change to another inclination, one can rescale by multiplying by  $(\sin 60/\sin i)^3$  and  $(\sin 60/\sin i)$  for masses and semi-major axis, respectively

Table 5 column 6 lists the distance from this relation based upon the physical radius in column 5. Columns 7 and 8 list the physical and angular semimajor axis of the binary, respectively, based upon the masses, period, and distance. The angular semimajor axis is approximately 0.5 mas in all three spin cases given in Table 5, which suggests that the binary is probably unresolved in the CHARA Array interferometric observations (Section 5). The luminosity of the visible star is large for the radii given in Table 5,  $\log L/L_\odot \approx 5.1 - 5.5$ , and if this is comparable to the initial luminosity of the star before mass transfer, then the star probably began life with a mass of  $\approx 20 - 30M_\odot$  (Saio et al. 2013).

All the results suggest that the system has gone through a mass reversal process in addition to the mass-loss from stellar winds and eruptions that caused the large ejecta seen by Marston & McCollum (2008). Our derived mass ratio would imply that the system is still early in the process of mass transfer, as it has yet to reach the more extreme values found in systems such as HDE 326823 ( $M_2/M_1 = 5.3$ ) or RY Scuti ( $M_2/M_1 = 3.9$ ), but the mass ratio is still clearly reversed. We also note that the observation of very strong Balmer line emission tells us that the primary star still has some hydrogen, supporting the idea that MWC 314 is not as far along in its binary interaction as the pre-(WN + O) binary, HDE 326823. If the low masses we derive are correct, then the Roche radius of the primary must be smaller than estimated by L13, making the primary less luminous and the distance smaller, as indicated in Table 5.

The visible star mass that we derive is surprisingly low for a star that has a spectrum resembling the prototypical LBV, P Cygni. The masses derived by L13 are much closer to expectations for an LBV mass, but we caution that their results are based upon the mass function from the radial velocity curve and an inclination and mass ratio estimated from fits of the light curve. Recall from Section 4.2 and Figure 2 that the light curve is complex and that a PHOEBE calculation with a large mass ratio  $q$  produces a light curve (Model #4) that is qualitatively similar to those for a small mass ratio (Models #1,2,3). Consequently, there is probably a large range in adopted mass ratios and hence masses (Fig. 6) that will yield model light curves similar to the observed photometric light curve. Our determination of the mass ratio (above) was made assuming synchronous rotation and a visible star that fills its Roche lobe at periastron. L13 recognised that their model implied slower than synchronous rotation for the visible star (they suggested a possible synchronous relation with gas forming the inner boundary of the circumbinary disc). However, stars that fill their Roche lobes experience strong tidal forces that drive the system towards synchronous rotation on a relatively short time scale,

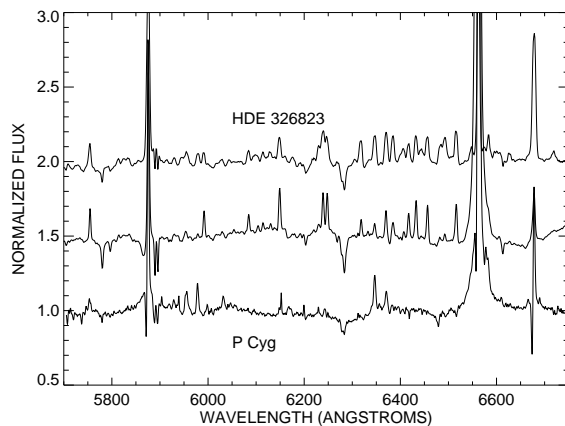


**Figure 8.** A comparison between the spectrum of MWC 314 (bold, center), HDE 326823 (Richardson et al. 2011; offset for clarity), and P Cygni (Richardson et al. 2013, bottom) shows that MWC 314 and HDE 326823 are nearly spectroscopic twins with the exception of the stronger hydrogen emission and lack of a few weak emission lines from MWC 314. Similarly, the comparison with P Cygni shows the similarity of the stellar winds of the two stars.

so the masses that we derive based upon the assumption of synchronous rotation are worthy of detailed consideration.

Note that we have made the assumption that the absorption lines we measured form in the atmosphere of the visible star. We suspect that the mass gainer in the system is surrounded by a thick gas torus (see below), and it is possible that the absorption lines form in this torus instead. If so, then the radial velocity curve would apply to the mass gainer and the identities of the stars would be swapped in the mass-mass diagram (Fig. 6). The measured “projected rotational velocity” in this case would correspond to Keplerian motion in the gas disc surrounding the mass gainer and not to the rotational broadening of the mass donor star, so the  $(v \sin i)/K_1$  argument would not apply. However, spectral lines formed in a torus surrounding the mass gainer have been detected for both  $\beta$  Lyr (Ak et al. 2007) and RY Scuti (Grundstrom et al. 2007), and in both these cases the lines display very large rotational broadening. Consequently, we suspect that the narrow absorption lines we observe in the spectrum of MWC 314 do not form in gas torus but are associated with the photosphere of the visible star.

## 6.2 Pulsational Behaviour

The *MOST* photometry presented us with an opportunity to explore the pulsational properties of this unusual system. In particular, a pulsational analysis may provide another clue that supports the relatively low mass of the visible star that we estimated above. We examined the pulsational stability of MWC 314 using the nonrotating stellar models and the modal analysis described by Saio et al. (2013). Saio et al. discuss how pulsations may be excited among blue supergiants in cases where the luminosity to mass ratio is large (for example, after extensive mass loss during a prior red supergiant phase). This is especially pertinent for MWC 314 if the stellar mass has decreased significantly through mass

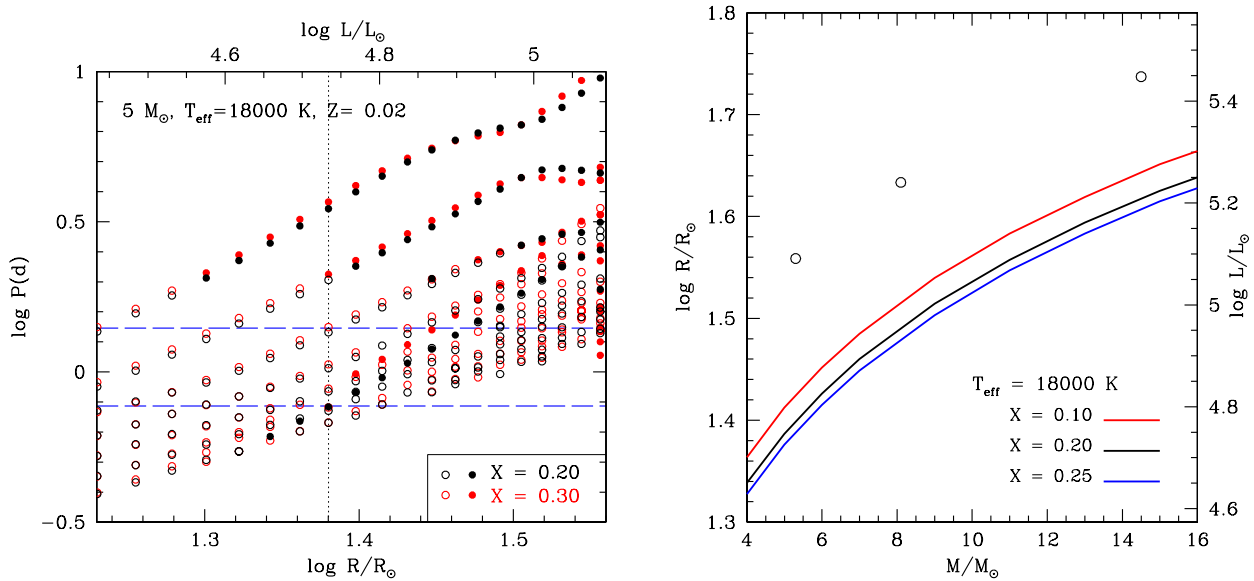


**Figure 7.** A comparison of the observed two periods (0.77 d and 1.4 d; horizontal dashed lines) with theoretical pulsation periods for models of a stellar mass of  $5M_{\odot}$  and an effective temperature of 18000 K with hydrogen mass fractions  $X=0.2$  (black symbols) and  $X=0.3$  (red symbols). Filled and open circles indicate excited and damped pulsation modes, respectively. The bottom and the top horizontal axes measure stellar radius and luminosity, respectively. The longest period of each model is the fundamental mode. We find that the observed dominant period ( $P=0.77$ d) is reproduced by an excited mode in a  $5M_{\odot}$  model at a radius of  $24 R_{\odot}$  ( $\log R/R_{\odot} = 1.38$ ; vertical dotted line) with  $X = 0.2$ . The second overtone of this model has a period of 1.4 d close to the observed second period, although the mode is not excited. We note that the model predicts the fundamental mode with a period of 3.5 d to be excited, although no such periodicity is detected from our *MOST* light curves. On the right panel, we show how the radius and luminosity scale with mass for the range of allowed masses (Section 6.1) and hydrogen fractions that can support this pulsational mode. The open circles denote the values derived by the Roche geometry analysis in Section 6.1 and Table 7.

**Table 6.** Models having an excited 0.77 d pulsation mode ( $X = 0.2$ ,  $Z = 0.02$ ,  $T_{\text{eff}} = 18,000$  K).

Mass ( $M_{\odot}$ )	Radius ( $R_{\odot}$ )	$\log(L/L_{\odot})$	Other excited period(s)	Period closest to 1.40 d <sup>†</sup>
4.0	21.5	4.64	1.98, 3.47 d	1.32 d
5.0	24.0	4.73	3.50 d	1.36 d
6.0	26.3	4.81	3.52 d	1.39 d
7.0	28.5	4.88	3.58 d	1.43 d
9.0	32.3	4.99	3.59 d	1.48 d

<sup>†</sup> Note that these periods are all second overtones, and all are damped.

transfer while maintaining the luminosity of the He-burning core.

We began by exploring what range of mass and radius would yield models with an excited mode pulsational period of 0.77 d for a stellar effective temperature of  $T_{\text{eff}} = 18000$  K. We found that there were no models with normal hydrogen abundances that could support the dominant pulsational model. However, if the hydrogen mass fraction  $X$  was set to a value less than 0.3, then we were able to find models with a pulsational frequency that matched the observed one. The parameters for these solution families are illustrated in Figure 7 (right panel) that plots the stellar mass, radius, and luminosity for several trial values of  $X$ . Figure 7 also shows the stellar parameters estimated above from the Roche geometry arguments (Table 5), and we see that these indicate an overluminosity for mass relative to the smallest hydrogen fraction family of pulsation models ( $X = 0.10$ ). It is possi-

ble that even lower hydrogen abundance models may excite pulsations like those observed, but it is difficult to specify the structure of the stellar envelope for such a stripped down star. This pulsational frequency is unlike frequencies often observed in LBVs, which are both longer time-scales and not strictly periodic (e.g., van Genderen 2001). The fundamental 0.77 d period is also shorter in duration than the dominant periods, and smaller in amplitude than the pulsational frequencies reported for 24 B supergiants reported by Lefever, Puls, & Aerts (2007).

The pulsation mode identified with the 0.77 d period of MWC 314 is a kind of strange mode associated with the He II ionization zone ( $\log T \approx 4.5$ ), and the amplitude is strongly confined to the outermost layers with  $\log T < 4.6$ . On the other hand, longer-period fundamental and first overtone modes with periods longer than a few days are excited by the  $\kappa$ -mechanism around the Fe-opacity peak at  $\log T \approx 5.3$

as occurs in other B-type variables with normal surface H-abundance. With a low hydrogen abundance of  $X \lesssim 0.25$ , the mode having a period of 0.77 d at  $T_{\text{eff}} = 18000$  K is excited by the  $\kappa$ -mechanism in the He II ionization zone for models with masses consistent with those from the orbital analysis, although the radius required for the period tends to be smaller than that of the critical Roche Lobe as shown in Figure 7 (right panel).

In Table 6, we summarize the models with  $X = 0.2$  in which the 0.77 d period is a supported pulsational mode. These models show that there is a family of lower-mass models in which this pulsational frequency is excited. The left hand panel of Figure 7 shows an example how the periods and the stability of the pulsation change for models with  $M = 5M_{\odot}$  as a function of radius at  $T_{\text{eff}} = 18000$  K. The model reproduces the 0.77 d period at  $\log R/R_{\odot} = 1.38$ . In addition, the period of the second overtone of these models falls in the range of 1.3 to 1.4 d, which is similar to the observed secondary period (1.4 d), although the mode is predicted to be damped. We note that these models predict that the fundamental mode with a period of  $\approx 3.5$  d should be excited, but we find no evidence of this periodicity in the *MOST* data (Fig. 3).

This pulsational analysis demonstrates that the kind of pulsational frequencies observed are broadly consistent with models in which the stellar mass is relatively small and the hydrogen abundance is low. This provides additional evidence that the visible star is the stripped-down remnant of binary mass transfer and that it is currently the lower mass component in the binary (Table 5).

### 6.3 Interferometry

The only LBV with comparable interferometric data is P Cygni (Richardson et al. 2013). The best models to reproduce the spherically symmetric wind of P Cyg were created either by the non-LTE code CMFGEN or a simple uniform disc surrounded by a Gaussian halo, and show that the  $H$ -band flux emerges from a halo about 2.4 times larger than the photosphere. In comparison, the emission from the  $K$ -band wind of MWC 314 is about 6 times larger than the photosphere for the case of MWC 314 (Model #3 in Table 4). Despite the differing wavelength of the observations for MWC 314 and P Cygni, the differences between the  $H$ - and  $K$ -bands are fairly small (a few percent in the case of the CMFGEN model of P Cygni computed by Najarro 2001). We note that optical polarimetric observations of MWC 314 show some evidence of a preferred direction (Wisniewski et al. 2006), which may in fact be emerging from the circumbinary disc component of the flux, rather than a wind asymmetry.

The largest remaining question is why the sizes are so different between P Cygni and MWC 314. The optical and near-infrared spectra appear similar (L13, Fig. 7), so we may suspect them to appear similar in physical size and geometry. However, in the case of an interacting binary many of the existing models for hot star winds may not be good approximations. We know that MWC 314 has a circumbinary disc, and it must account for some of the flux we see with the CHARA Array. However, we had a difficult time discerning different models of the visibilities, other than the extended halo of light surrounding the system. It's large size compared

to P Cygni likely indicates that the CHARA Array is seeing evidence of both the wind and the disc.

The large halo observed with CHARA likely has an origin in both a large circumbinary disc and a circumbinary wind, and there is evidence from spectroscopy that the binary is embedded in a disc. The appearance of strong emission lines throughout the optical and near-infrared spectrum of MWC 314 indicates the presence of circumstellar gas from ongoing mass loss. With the exception of the strong Balmer lines and He I emission lines, the optical emission lines tend to be weakly ionised metal lines, such as Fe II. These lines exhibit double-peaked profiles (Miroshnichenko et al. 1998) that are stationary in radial velocity (L13), indicative of an origin in a circumbinary disc rather than in either star. The same double-peaked and stationary emission lines are found in the spectrum of the spectroscopic binary HDE 326823. Richardson et al. (2011) argue that these lines form in a circumbinary disk that is fed by mass loss from the binary. The visible star in HDE 326823 is losing mass to a hidden secondary star via Roche lobe Overflow (RLOF) and losing mass to the circumbinary disk by outflow through L2. In fact, the spectral similarities of the two stars are remarkable. In Figure 7, we show a comparison of the average low resolution spectrum of HDE 326823 (Richardson et al. 2011) and a similar resolution spectrum of MWC 314 we obtained at the Observatoire du Mont Mégantic. With the exception of the stronger  $H\alpha$  line in MWC 314 and the absence of a few weak emission lines, the stars can be considered spectroscopic twins. HDE 326823 is an example of a W Serpentis binary (Tarasov 2000), where a less-massive primary star has lost mass onto a secondary star hidden behind an optically thick accretion torus (Nazarenko & Glazunova 2006). In these systems, mass exchange and systemic mass loss have drastically altered the stellar masses.

## 7 SUMMARY AND FUTURE WORK

With the recent discovery that the LBV candidate HDE 326823 is an interacting binary and with the work presented here and in L13 on MWC 314, we now have two candidate LBVs that are probably interacting binaries. Plavec (1980) and Tarasov (2000) show that the W Serpentis binaries can have a mass-loss and transfer rate up to  $10^{-4} M_{\odot} \text{yr}^{-1}$ , which is comparable to the mass-loss rates of LBVs. However, we caution that mass-loss via a stellar wind and mass transfer are very different processes, which may have very different mass-loss rates. The spectral appearance of double-peaked emission lines in these highly luminous stars may be an observational way to find more interacting binaries in the future, so that high spectral resolution time-series observations will help to distinguish between LBVs and mass-transferring binaries. MWC 314 and HDE 326823 are the only two known LBV candidates that show double-peaked emission, but others may be found in the future as massive stars identified through infrared surveys (e.g., Wachter et al. 2010; Stringfellow et al. 2012) are examined at higher spectral resolution. For example, the supergiant B[e] star (sgB[e]) Wd1-9 may show similar properties to HDE 326823 and MWC 314 (Clark et al. 2013).

In summary, we found the following properties related to the interacting binary MWC 314.

(i) MWC 314 is a single-lined spectroscopic binary with a period of 60.753 d and a moderate eccentricity ( $e = 0.29$ ). The full orbital parameters are given in Table 1.

(ii) The system shows photometric variability modulated with the orbital period. We constructed light curve models for the tidal deformation of the star around periastron that were made with the period, epoch, eccentricity, and longitude of periastron set from the spectroscopic results. The model light curves capture the main features of the orbital light curve (timing and number of maxima), but the model over- and under-predicts the flux just before and after visible star inferior conjunction, respectively. We suspect that these differences are related to wind and/or disc asymmetries that are not included in the PHOEBE model of the light curve. Solutions similar to that of L13 can be found with both large and small masses.

(iii) With the *MOST* photometry, we discovered two pulsational periods in the system. These periods cannot be supported in a star with parameters (mass, radius) of a typical LBV, but can easily represent a hydrogen-poor, low-mass star.

(iv) From the CHARA Array measurements of the squared visibility of the system, we found that a halo of light around the binary is partially resolved. We argue that the angular size of the halo is too large for the wind alone, and it probably represents the flux of the wind and circumbinary disc.

(v) We demonstrated how a consideration of the Roche geometry can be used to derive the mass ratio from the observed ratio of projected rotational velocity to orbital semi-amplitude (independent of the system inclination). If we assume that the visible star spins with the same angular rate as the orbital advance at periastron, then we derive a mass ratio  $q = M_2/M_1 = 2.36$ , indicating that the donor star is now the lower mass component in the binary. We consider other cases in which the spin rate is lower, but the mass ratio is limited to  $q > 1.32$  if we accept models that predict a growth in eccentricity with mass transfer (Sepinsky et al. 2007a, 2009). There is a factor of 3 – 10 discrepancy between the masses of the L13 study and ours. This discrepancy could be resolved with the appropriate observations in the future that spectroscopically determine the secondary radial velocity curve. However, that may not be possible if the secondary is hidden in an accretion torus.

The system presents opportunities to study mass transfer with multiple observing strategies. Further efforts should be employed to obtain very high signal-to-noise spectroscopy with high spectral resolution. Such spectroscopy may reveal the nature of the newly-discovered pulsational modes over short time-scales or find a spectroscopic signature of the companion over orbital time-scales. The analysis of the interferometry may be able to be improved if a near-infrared light curve is measured for the system, which we have begun trying to do with the CPAPIR instrument (Artigau et al. 2004). This would allow us to account for any changes with orbital phase in the ratio of central binary to surrounding flux, which would lead to an improved interpretation of the interferometric results. A combination of this with the distance to MWC 314 with the recently launched GAIA satellite will provide constraints on the physical size of the outflow, allowing us to better understand mass exchange in

this binary system. All of these analyses will yield insights into the physics of the system which likely includes RLOF and accretion, and which could include either a circumbinary disc or jets. MWC 314 is an exciting target for our understanding of post-main sequence binary interactions of massive stars.

## ACKNOWLEDGEMENTS

We thank the anonymous referee for helping the analysis and presentation of this paper. We are grateful to Fred Walter (Stony Brook University) for his scheduling of spectroscopic observations with the CTIO 1.5 m, to the CTIO SMARTS staff for queue observing support, and to Todd Henry (Georgia State University) for assistance in scheduling the initial observations with the SMARTS echelle spectrograph. We are also grateful to John Monnier (Univ. of Michigan) for contributions to data reduction and analysis. We thank Pierre-Luc Lévesque, Bernard Malenfant, Ghislain Turcotte, and Philippe Vallée for their assistance in obtaining data at the Observatoire du Mont Mégantic. Some spectra with the CTIO 1.5 m were obtained through the NOAO Programs 2009B-0153 and 2012A-0216. This work was partially based on observations obtained at the 2.1-m Otto Struve and 2.7-m Harlan. J. Smith telescopes of the McDonald Observatory of the University of Texas at Austin. This work was also based partially on observations obtained at the Mercator telescopes and HERMES spectrograph of the Instituto de Astrofísica de Canarias. This research was made possible through the use of the AAVSO Photometric All-Sky Survey (APASS), funded by the Robert Martin Ayers Sciences Fund. Operational funding for the CHARA Array is provided by the GSU College of Arts and Sciences, by the National Science Foundation through grants AST-0606958, AST-0908253, and AST-1211129, by the W. M. Keck Foundation, and by the NASA Exoplanet Science Institute. We thank the Mount Wilson Institute for providing infrastructure support at Mount Wilson Observatory. The CHARA Array, operated by Georgia State University, was built with funding provided by the National Science Foundation, Georgia State University, the W. M. Keck Foundation, and the David and Lucile Packard Foundation. This research has made use of the SIMBAD database, operated at CDS, Strasbourg, France.

NDR is grateful for his CRAQ (Centre de Recherche en Astrophysique du Québec) postdoctoral fellowship. AFJM and NSL are grateful for financial support from NSERC (Canada) and FRQNT (Québec). DRG and GS acknowledge support from NSF grant AST-1411654. AM and SZ acknowledge support from DGAPA/PAPIIT project IN100614. TSB acknowledges support provided through NASA grant ADAP12-0172.

## REFERENCES

- Ak, H., Chadima, P., Harmanec, P., Demircan, O., et al. 2007, *A&A*, 463, 233
- Artigau, É., Doyon, R., Vallee, P., et al., 2004, in Society of Photo-Optical Instrumentation Engineers (SPIE) Conference Series, Vol. 5492, Society of Photo-Optical Instrumentation Engineers (SPIE) Conference Series, 1459

- Baines, E. K., McAlister, H. A., ten Brummelaar, T. A., et al. 2010, *AJ*, 140, 167
- Barden, S. C. & Ingerson, T. E. 1998, in *Fiber Optics in Astronomy III* (ASP Conf. Vol. 152), ed. S. Arribas, E. Mediavilla, & F. Watson (San Francisco: ASP), 60
- Beech, M. 1985, *Ap&SS*, 117, 69
- Berger, D. H., Gies, D. R., McAlister, H. A., et al. 2006, *ApJ*, 644, 475
- Boyajian, T. S., McAlister, H. A., van Belle, G., et al. 2012, *ApJ*, 746, 101
- Cannon, A. J., 1925, *Ann. Astron. Obs. Harvard Coll.*, 100, 17
- Chentsov, E. L., Ermakov, S. V., Klochkova, V. G., et al. 2003, *A&A*, 397, 1035
- Clark, J. S., Ritchie, B. W., & Negueruela, I. 2013, *A&A*, 560, 11
- Clemens, D. P., Sarcia, D., Grabau, A., et al. 2007, *PASP*, 119, 1385
- Davis, J., Tango, W. J., & Booth, A. J. 2000, *MNRAS*, 318, 387
- Eggleton, P. P. 1983, *ApJ*, 268, 368
- Fitzpatrick, E. L. 1999, *PASP*, 111, 63
- Gies, D. R., & Bolton, C. T. 1986, *ApJ*, 304, 371
- Groh, J. H., Meynet, G., Georgy, C., & Ekström, S. 2013, *A&A*, 558, 131
- Grundstrom, E. D., Gies, D. R., Hillwig, T. C., et al. 2007, *ApJ*, 667, 505
- Humphreys, R. M., & Davidson, K. 1994, *PASP*, 106, 1025
- Kent, S. M. 1985, *PASP*, 97, 165
- Koenigsberger, G., Georgiev, L., Hillier, D. J., et al. 2010, *AJ*, 139, 2600
- Lefever, K., Puls, J., & Aerts, C. 2015, *A&A*, 463, 1093
- Lenz P., & Breger M. 2005, *Commun. Asteroseismol.*, 146, 53
- Liermann, A., Schnurr, O., Kraus, M., Kreplin, A., Arias, M. L., Cidale, L. S. 2014, *MNRAS*, 443, 947
- Lobel, A., Groh, J. H., Martayan, C., et al. 2013, *A&A*, 559, 16 (L13)
- Lobel, A., Martayan, C., Corcoran, M., Groh, J. H., & Frémat, Y. 2015, in *New windows on massive stars: asteroseismology, interferometry, and spectropolarimetry*, IAU Symp. 307, ed. G. Meynet, C. Georgy, J. Groh, & P. Stee (Cambridge, UK: Cambridge Univ. Press), 115
- Madura, T. I., Gull, T. R., Okazaki, A. T., et al. 2013, *MNRAS*, 436, 3820
- Marston, A. P., & McCollum, B. 2008, *A&A*, 477, 193
- Martayan, C., Lobel, A., Baade, D. et al. 2012, in *Astronomical Society of the Pacific Conference Series*, Vol. 464, *Circumstellar Dynamics at High Resolution*, ed. A. C. Carciofi & T. Rivinius, (San Francisco: ASP) 293
- Mason, B. D., Hartkopf, W. I., Gies, D. R., Henry, T. J., & Helsel, J. W. 2009, *AJ*, 137, 3358
- Miroshnichenko, A. S. 1996, *A&A*, 312, 941
- Miroshnichenko, A. S., Fremat, Y., Houziaux, L., et al. 1998, *A&AS*, 131, 469
- Muratorio, G., Rossi, C., & Friedjung, M., 2008, *A&A*, 487, 637
- Najarro, F. 2001, in *P Cygni 2000: 400 Years of Progress* (ASP Conf. Vol. 233), ed. M. de Groot & C. Sterken (San Francisco: ASP), 133
- Nazarenko, V. V., & Glazunova, L. V. 2006, *Astr. Rep.*, 50, 369
- Pauls, T. A., Young, J. S., Cotton, W. D., & Monnier, J. D. 2005, *PASP*, 117, 1255
- Plavec, M. J. 1980, in *Close binary stars: Observations and interpretation*, ed. M. J. Plavec, D. M. Popper, & R. K. Ulrich (Dordrecht: Reidel Publ.), 251
- Pojmański, G. 2002, *Acta. Astron.*, 52, 397
- Prša, A., & Zwitter, T. 2005, *ApJ*, 628, 426
- Raskin, G., van Winckel, H., Hensberge, H., et al., 2011, *A&A*, 526, A69
- Richardson, N. D., Gies, D. R., Henry, T. J., Fernández-Lajús, E., & Okazaki, A. T., 2010, *AJ*, 139, 1534
- Richardson, N. D., Gies, D. R., & Williams, S. J., 2011, *AJ*, 142, 201
- Richardson, N. D., Schaefer, G. H., Gies, D. R., et al. 2013, *ApJ*, 769, 118
- Saio, H., Georgy, C., & Meynet, G. 2013, *MNRAS*, 433, 1246
- Saio, H., Kuschnig, R., Gautschi, A. et al. 2006, *ApJ*, 650, 111
- Sana, H., de Mink, S. E., de Koter, A., et al. 2012, *Science*, 337, 444
- Scargle, J. D. 1982, *ApJ*, 263, 835
- Schaefer, G. H., Gies, D. R., Monnier, J. D., et al. 2010, *AJ*, 140, 1838
- Schaefer, G. H., ten Brummelaar, T., Gies, D. R., et al. 2014, *Nature*, 515, 234
- Sepinsky, J. F., Willems, B., & Kalogera, V. 2007b, *ApJ*, 660, 1624
- Sepinsky, J. F., Willems, B., Kalogera, V., & Rasio, F. A. 2007a, *ApJ*, 667, 1170
- Sepinsky, J. F., Willems, B., Kalogera, V., & Rasio, F. A. 2009, *ApJ*, 702, 1387
- Sepinsky, J. F., Willems, B., Kalogera, V., & Rasio, F. A. 2010, *ApJ*, 724, 546
- Stringfellow, G. S., Gvaramadze, V. V., Beletsky, Y., & Kniazev, A. Y. 2012, in *Four Decades of Research on Massive Stars, A Meeting in Honor of Anthony F. J. Moffat* (ASP Conf. Vol. 465), ed. L. Drissen, C. Robert, N. St.-Louis, & A. F. J. Moffat (San Francisco: ASP), 514
- Tarasov, A. E. 2000, in *The Be Phenomenon in Early-Type Stars* (ASP Conf. Ser. 214), ed. M. A. Smith, H. F. Henrichs, & J. Fabregat (San Francisco: ASP), 644
- ten Brummelaar, T. A., McAlister, H. A., Ridgway, S. T., et al. 2005, *ApJ*, 628, 453
- ten Brummelaar, T. A., Sturmman, J., Ridgway, S. T., et al. 2013, *JAI*, 02, 1340004
- Tokovinin, A., Fischer, D. A., Bonati, M., et al. 2013, *PASP*, 125, 1336
- Touhami, Y., Gies, D. R., Schaefer, G. H., et al. 2013, *ApJ*, 768, 128
- Tubbesing, S., Kaufer, A., Stahl, O., et al. 2002, *A&A*, 389, 931
- Vacca, W. D., Cushing, M. C., & Rayner, J. T. 2003, *PASP*, 115, 389
- van Belle, G. T., van Belle, G., Creech-Eakman, M. J., et al. 2008, *ApJS*, 176, 276
- van Genderen, A. M., 2001, *A&A*, 366, 508
- Vanbeveren, D., & Conti, P. S., 1980, *A&A*, 88, 230
- Walker, G., Matthews, J., Kuschnig, R., et al. 2003, *PASP*, 115, 1023
- Wachter, S., Mauerhan, J. C., Van Dyk, S. D., et al. 2010, *AJ*, 139, 2330
- Windhorst, R. A., Burstein, D., Mathis, D. F., et al. 1991, *ApJ*, 380, 362
- Wisniewski, J. W., Babler, B. L., Bjorkman, K. S., et al. 2006, *PASP*, 118, 820

## APPENDIX A: SUPPLEMENTARY MATERIAL

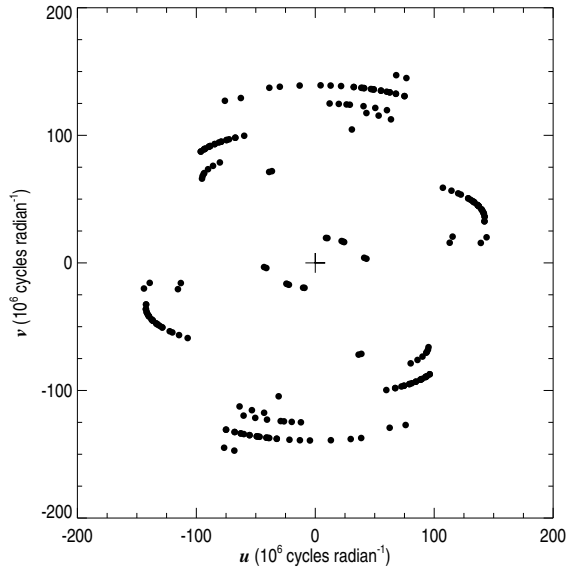
This paper has been typeset from a  $\text{\TeX}$ / $\text{\LaTeX}$  file prepared by the author.

**Table A1.** Spectroscopic Observing Log

Telescope	Spectrograph	Range ( $\text{\AA}$ )	$R$	$N_{\text{spectra}}$	HJD (first)	HJD (last)
Struve 2.1 m	Sandiford Cassegrain Echelle	5600–6800	60,000	2	2452192.6	2452542.6
Harlan Smith 2.7 m	TS2 Echelle Spectrograph	3600–9875	60,000	1	2455082.7	...
CTIO 1.5 m	SMARTS Fiber echelle	4800–7200	40,000	7	2455429.6	2455449.5
CTIO 1.5 m	CHIRON echelle	4500–8500	28,000	4	2456029.9	2456079.8
Mercator 1.2 m	HERMES Spectrograph	3800–8750	50,000	3	2456053.6	2456133.5
OMM 1.6 m	Cassegrain, 1200 g mm <sup>-1</sup> grating	4500–6700	3,200	2	2456489.6	2456494.7
San Pedro Martir 2.1 m	Echelle REOSC	4600–8100	18,000	1	2456587.6	...

**Table A2.** CHARA Interferometric Observing Log

UT Date	Beam Combiner	Baseline(s)	Baseline Length(s) [m]	$N_{\text{observations}}$	Calibrator HD number(s)
2010 Sep 04	Classic	S2/E2	248	1	182101
2010 Sep 05	Classic	S2/W2, W1/W2	177, 107	2, 2	174897
2010 Sep 21	Classic	E1/E2	65	2	182101
2010 Sep 22	Classic	E1/E2	65	2	174897
2011 Sep 25	CLIMB	S2/W1/E1	249, 313, 302	4	182101
2012 Jul 06	Classic	S1/E1	330	6	182101, 184606
2012 Jul 08	CLIMB	S1/E1/W1	330, 313, 278	2	182101, 184606
2012 Aug 02	CLIMB	S1/E1/W1	330, 313, 278	5	182101
2012 Sep 16	CLIMB	S1/E1/W1	330, 313, 278	5	182101, 184606
2012 Sep 22	CLIMB	S1/E1/W1	330, 313, 278	5	182101, 184606
2013 Aug 13	CLIMB	S1/E2/W1	278, 251, 278	2	174897, 182101
2013 Aug 13	Classic	S1/E2	278	1	174897
2013 Oct 01	CLIMB	S1/E1/W1	330, 313, 278	2	182101, 184606

**Figure A1.**  $(u, v)$  sampling of the CHARA measurements, showing that the observations sample many different baselines and position angles on the sky.



**Table A3.** New Radial Velocity Measurements

HJD -2,450,000	$V_r$ (km s $^{-1}$ )	Phase	Telescope
2192.6045	+70.7	0.604	McDonald Observatory
2542.6229	+93.0	0.365	McDonald Observatory
5082.6760	+57.9	0.174	McDonald Observatory
5429.5890	-52.0	0.884	CTIO SMARTS echelle
5430.6169	-64.9	0.901	CTIO SMARTS echelle
5444.4983	+29.8	0.130	CTIO SMARTS echelle
5445.4805	+45.6	0.146	CTIO SMARTS echelle
5446.4785	+45.4	0.162	CTIO SMARTS echelle
5447.4750	+63.9	0.179	CTIO SMARTS echelle
5449.5198	+81.8	0.212	CTIO SMARTS echelle
6029.8825	+10.1	0.765	CTIO CHIRON
6053.6094	+51.3	0.156	Mercator-HERMES
6054.8914	+73.6	0.177	CTIO CHIRON
6078.8322	+78.7	0.571	CTIO CHIRON
6079.8378	+87.9	0.587	CTIO CHIRON
6103.4839	-67.5	0.977	Mercator-HERMES
6133.5428	+95.0	0.471	Mercator-HERMES
6489.6439	+92.8	0.333	Observatoire du Mont Mégantic
6494.7573	+95.8	0.417	Observatoire du Mont Mégantic
6587.5821	-88.5	0.945	SPM echelle

**Table A4.** Ground-based Photometric Measurements

HJD -2,450,000	<i>B</i>	$\sigma_B$	<i>V</i>	$\sigma_V$	<i>R</i>	$\sigma_R$	<i>I</i>	$\sigma_I$
5275.011	11.899	0.008	10.135	0.005	8.607	0.004	7.437	0.004
5280.941	11.892	0.007	10.116	0.016	8.578	0.004	7.441	0.008
5291.996	11.904	0.006	10.153	0.004	8.615	0.004	7.486	0.004
5294.886	11.964	0.007	10.173	0.010	8.624	0.032	7.491	0.009
5298.875	11.960	0.012	10.181	0.029	8.630	0.012	7.492	0.024
5312.838	11.916	0.006	10.141	0.012	8.598	0.009	7.465	0.005
5321.808	11.972	0.019	10.206	0.059	8.650	0.013	7.491	0.011
5324.800	11.955	0.007	10.180	0.005	8.599	0.014	7.471	0.010
5327.801	11.897	0.011	10.143	0.048	8.609	0.014	7.444	0.007
5330.792	11.878	0.024	10.134	0.025	8.588	0.036	7.449	0.018
5333.778	11.897	0.006	10.121	0.037	8.581	0.031	7.429	0.004
5337.879	11.889	0.007	10.104	0.004	8.568	0.012	7.422	0.004
5340.898	11.890	0.005	10.101	0.018	8.569	0.005	7.411	0.010
5352.873	11.962	0.016	10.178	0.009	8.641	0.007	7.495	0.004
5359.879	11.973	0.005	10.183	0.011	8.648	0.012	7.493	0.004
5362.871	11.979	0.005	10.186	0.022	8.650	0.010	7.505	0.014
5365.869	11.966	0.017	10.203	0.004	8.647	0.024	7.509	0.010
5368.826	11.975	0.005	10.183	0.025	8.656	0.004	7.505	0.014
5382.796	12.018	0.015	10.222	0.015	8.666	0.027	7.520	0.016
5455.716	11.898	0.019	10.132	0.009	8.607	0.004	7.455	0.019
5468.691	11.922	0.029	10.157	0.008	8.610	0.021	7.484	0.010
5471.712	11.897	0.012	10.140	0.004	8.587	0.022	7.472	0.004
5476.705	11.942	0.007	10.161	0.008	8.633	0.019	7.490	0.015
5479.685	11.967	0.031	10.197	0.017	8.644	0.004	7.513	0.009
5498.622	11.905	0.005	10.139	0.005	8.601	0.004	7.457	0.008
5506.596	11.943	0.020	10.168	0.010	8.626	0.004	7.489	0.004
5511.621	11.915	0.005	10.120	0.032	8.587	0.022	7.451	0.010
5604.032	11.971	0.006	10.211	0.031	8.649	0.008	7.514	0.012
5610.016	11.991	0.011	10.213	0.012	8.695	0.045	7.533	0.063
5621.982	11.974	0.009	10.178	0.004	8.636	0.011	7.492	0.011
5624.975	11.979	0.023	10.205	0.037	8.623	0.030	7.496	0.046
5631.956	11.916	0.008	10.137	0.044	8.598	0.043	7.439	0.022
5634.948	11.891	0.021	10.106	0.022	8.564	0.016	7.431	0.016
5637.940	11.900	0.008	10.113	0.015	8.597	0.005	7.421	0.047
5644.921	11.944	0.006	10.155	0.013	8.600	0.004	7.474	0.004
5648.911	11.945	0.021	10.160	0.033	8.589	0.016	7.475	0.006
5653.897	11.920	0.006	10.157	0.005	8.617	0.005	7.477	0.021
5663.871	11.987	0.007	10.183	0.016	8.644	0.016	7.489	0.023
5667.861	11.996	0.007	10.204	0.006	8.672	0.031	7.528	0.009
5671.850	11.976	0.007	10.185	0.029	8.664	0.031	7.524	0.041
5679.829	11.916	0.009	10.138	0.005	8.604	0.019	7.493	0.019
5685.812	11.978	0.023	10.197	0.028	8.634	0.051	7.509	0.010
5688.931	11.948	0.010	10.155	0.007	8.610	0.004	7.469	0.004
5694.915	11.927	0.013	10.137	0.004	8.609	0.017	7.457	0.019
5697.781	11.872	0.008	10.108	0.005	8.551	0.010	7.452	0.004
5712.845	11.885	0.006	10.113	0.009	8.584	0.012	7.446	0.008
5721.891	11.988	0.043	10.190	0.022	8.646	0.010	7.516	0.006
5725.822	11.996	0.031	10.226	0.026	8.665	0.020	7.519	0.010
5728.857	11.977	0.016	10.199	0.023	8.665	0.027	7.531	0.005
5735.852	11.921	0.013	10.136	0.014	8.609	0.004	7.483	0.006
5738.824	11.958	0.027	10.173	0.005	8.634	0.015	7.478	0.017
5741.951	11.945	0.022	10.173	0.008	8.607	0.007	7.491	0.016
5831.698	11.934	0.006	10.155	0.014	8.620	0.019	7.494	0.004
5835.692	11.944	0.008	10.165	0.031	8.616	0.004	7.518	0.028
5844.635	11.980	0.006	10.193	0.013	8.653	0.015	7.522	0.006
5850.630	11.962	0.045	10.197	0.008	8.650	0.005	7.524	0.004
5853.668	11.948	0.006	10.167	0.016	8.628	0.008	7.502	0.004
5858.684	11.897	0.008	10.127	0.009	8.585	0.004	7.477	0.004
5863.601	11.929	0.006	10.139	0.010	8.607	0.004	7.482	0.007
5867.600	12.005	0.007	10.202	0.005	8.661	0.027	7.520	0.007
5875.584	11.893	0.018	10.135	0.005	8.605	0.021	7.466	0.004
5883.601	11.882	0.006	10.117	0.005	8.567	0.005	7.452	0.009
6002.003	11.901	0.006	10.126	0.005	8.597	0.005	7.436	0.004
6035.987	11.979	0.023	10.180	0.020	8.645	0.004	7.503	0.024

**Table A4** – *continued* Photometric Measurements

JD - 2,450,000	$B$	$\sigma_B$	$V$	$\sigma_V$	$R$	$\sigma_R$	$I$	$\sigma_I$
6039.979	11.945	0.006	10.155	0.005	8.624	0.008	7.486	0.009
6042.906	11.934	0.006	10.136	0.009	8.609	0.011	7.463	0.008
6045.979	11.947	0.012	10.158	0.005	8.628	0.005	7.480	0.004
6048.878	11.989	0.016	10.211	0.015	8.651	0.039	7.514	0.038
6052.941	11.953	0.015	10.174	0.005	8.633	0.004	7.499	0.017
6067.970	11.899	0.011	10.118	0.006	8.588	0.010	7.457	0.033
6070.836	11.866	0.017	10.090	0.006	8.566	0.018	7.427	0.005
6073.836	11.919	0.008	10.138	0.038	8.609	0.009	7.449	0.019
6076.864	11.898	0.019	10.120	0.017	8.560	0.036	7.442	0.027
6086.868	11.942	0.007	10.155	0.018	8.640	0.027	7.484	0.005
6089.838	11.959	0.017	10.180	0.032	8.652	0.017	7.481	0.011
6092.845	11.987	0.008	10.180	0.005	8.650	0.005	7.507	0.005
6097.826	11.982	0.016	10.193	0.005	8.655	0.005	7.503	0.005
6104.847	11.937	0.009	10.123	0.008	8.596	0.004	7.460	0.019
6190.733	11.933	0.030	10.158	0.006	8.627	0.004	7.489	0.012
6193.640	11.966	0.022	10.166	0.004	8.630	0.011	7.489	0.013
6202.693	11.975	0.012	10.176	0.005	8.660	0.022	7.526	0.004
6205.610	11.964	0.009	10.169	0.011	8.646	0.004	7.515	0.008

**Table A5.**  $V^2$  Measurements from CHARA

HJD - 2,450,000 (d)	Baseline (m)	$u$ ( $10^6$ cycles $\text{radian}^{-1}$ )	$v$ ( $10^6$ cycles $\text{radian}^{-1}$ )	$V^2$	$\sigma_{V^2}$
5442.6938	232.508	65.653	223.046	0.552	0.043
5443.7053	171.935	-77.714	153.369	0.706	0.130
5443.7152	173.105	-82.696	152.075	0.622	0.079
5443.7943	92.0942	91.829	6.9727	1.096	0.085
5443.8059	88.1392	87.721	8.5707	1.026	0.165
5459.7630	46.8597	-21.801	-41.479	1.297	0.059
5459.7695	45.9541	-19.270	-41.718	1.216	0.239
5460.6517	62.3953	-51.795	-34.790	0.869	0.053
5460.6600	61.4734	-50.210	-35.467	0.959	0.048
5460.6741	59.7343	-47.242	-36.556	0.874	0.054
5828.6275	239.741	-171.085	167.945	0.415	0.074
5828.6275	312.117	299.632	87.394	0.573	0.052
5828.6275	285.871	-128.547	-255.339	0.427	0.097
5828.6472	244.850	-183.352	162.276	0.471	0.173
5828.6472	306.665	290.973	96.840	0.505	0.100
5828.6472	280.577	-107.621	-259.116	0.439	0.067
5828.6657	248.009	-192.273	156.651	0.454	0.075
5828.6657	298.036	278.787	105.372	0.527	0.122
5828.6657	275.937	-86.514	-262.023	0.454	0.125
5828.6860	249.381	-199.063	150.217	0.378	0.045
5828.6860	284.970	261.066	114.248	0.596	0.047
5828.6860	271.636	-62.003	-264.465	0.421	0.044
5842.6526	249.360	-200.189	148.677	0.579	0.082
5842.6526	281.406	256.275	116.243	0.611	0.050
5842.6526	270.793	-56.086	-264.921	0.508	0.072
5842.6636	248.785	-202.104	145.079	0.620	0.084
5842.6636	272.484	244.283	120.720	0.782	0.053
5842.6636	269.125	-42.178	-265.800	0.690	0.084
5842.6765	247.165	-203.101	140.857	0.423	0.057
5842.6765	261.055	228.827	125.650	0.416	0.134
5842.6765	267.746	-25.726	-266.507	0.526	0.066
6113.9098	299.267	46.283	295.666	0.564	0.049
6113.9224	297.775	27.543	296.499	0.706	0.219
6113.9357	297.049	9.5499	296.896	0.637	0.053
6113.9644	297.802	-27.985	296.484	0.553	0.098
6113.9897	301.286	-63.571	294.503	0.546	0.072
6114.0032	304.142	-82.374	292.775	0.731	0.049

**Table A5** – *continued*  $V^2$  Measurements from CHARA

HJD - 2,450,000 (d)	Baseline (m)	$u$ ( $10^6$ cycles $\text{radian}^{-1}$ )	$v$ ( $10^6$ cycles $\text{radian}^{-1}$ )	$V^2$	$\sigma_{V^2}$
6115.8049	253.758	-143.509	209.280	0.502	0.050
6115.8049	311.297	303.419	69.592	0.427	0.044
6115.8049	321.467	-159.909	-278.873	0.567	0.079
6115.8205	259.808	-159.041	205.441	0.567	0.076
6115.8205	313.415	303.733	77.297	0.432	0.063
6115.8205	317.611	-144.691	-282.738	0.524	0.096
6140.7364	253.672	-143.281	209.331	0.458	0.096
6140.7364	311.248	303.393	69.484	0.440	0.101
6140.7364	321.518	-160.111	-278.816	0.354	0.045
6140.7525	259.899	-159.272	205.378	0.475	0.098
6140.7525	313.426	303.715	77.417	0.572	0.119
6140.7525	317.548	-144.443	-282.795	0.516	0.047
6140.7679	265.385	-173.021	201.228	0.340	0.075
6140.7679	312.850	301.090	84.971	0.490	0.101
6140.7679	313.546	-128.068	-286.199	0.291	0.046
6140.7903	272.028	-190.032	194.645	0.446	0.048
6140.7903	307.525	292.246	95.729	0.401	0.045
6140.7903	307.839	-102.213	-290.374	0.444	0.092
6140.8049	275.251	-199.105	190.053	0.437	0.047
6140.8049	301.327	283.350	102.522	0.632	0.296
6140.8049	304.462	-84.244	-292.575	0.433	0.114
6185.6400	263.669	-168.728	202.613	0.410	0.048
6185.6400	313.319	302.256	82.525	0.456	0.151
6185.6400	314.855	-133.527	-285.139	0.362	0.075
6185.6541	268.295	-180.351	198.634	0.383	0.059
6185.6541	311.321	298.218	89.369	0.396	0.154
6185.6541	311.189	-117.866	-288.004	0.320	0.054
6185.6652	271.464	-188.534	195.313	0.395	0.047
6185.6652	308.272	293.367	94.695	0.411	0.051
6185.6652	308.375	-104.832	-290.009	0.419	0.090
6185.6794	274.749	-197.609	190.886	0.445	0.086
6185.6794	302.583	285.112	101.327	0.506	0.074
6185.6794	305.034	-87.502	-292.214	0.896	0.346
6185.6939	277.109	-205.261	186.165	0.499	0.141
6185.6939	294.781	274.330	107.884	0.495	0.090
6185.6939	302.052	-69.068	-294.049	0.519	0.110
6516.6622	275.739	135.758	240.003	0.685	0.078
6516.6923	271.208	113.641	246.250	0.592	0.068
6516.6923	243.414	-241.071	-33.697	0.943	0.208
6516.6923	247.825	127.429	-212.553	0.666	0.060
6516.7182	266.829	91.736	250.564	0.534	0.076
6516.7182	250.177	-246.290	-43.932	0.382	0.233
6516.7182	258.037	154.553	-206.631	0.560	0.097
6517.6701	274.233	128.202	242.421	0.684	0.130
6517.6701	234.346	-232.877	-26.192	0.594	0.203
6517.6701	240.233	104.675	-216.229	0.695	0.101
6517.6893	271.252	113.856	246.200	0.845	0.080
6517.6893	243.311	-240.982	-33.591	0.796	0.153
6517.6893	247.717	127.125	-212.609	0.390	0.087
6565.6292	272.530	-191.380	194.027	0.510	0.059
6565.6292	306.793	291.163	96.677	0.568	0.072
6565.6292	307.352	-99.782	-290.704	0.517	0.053
6565.6431	275.502	-199.870	189.613	0.453	0.158
6565.6431	300.639	282.391	103.146	0.867	0.217
6565.6431	304.168	-82.520	-292.760	0.459	0.168

Table A6. Orbital light curve from *MOST*

JD - 2,450,000	Phase	$\Delta m$ (mag)	JD - 2,450,000	Phase	$\Delta m$ (mag)	JD - 2,450,000	Phase	$\Delta m$ (mag)
6827.5752	0.9074	0.00820	6832.1544	0.9828	-0.00442	6836.3796	0.0524	0.00816
6827.6452	0.9085	0.00802	6832.2234	0.9839	0.00577	6836.4493	0.0535	0.00706
6827.7156	0.9097	0.00795	6832.2936	0.9851	0.00772	6836.5224	0.0547	0.01426
6827.7864	0.9109	0.01235	6832.3650	0.9863	-0.01125	6836.5842	0.0557	0.01600
6827.8569	0.9120	0.01427	6832.4349	0.9874	-0.01242	6836.6535	0.0569	0.02378
6827.9273	0.9132	0.01204	6832.5051	0.9886	-0.01085	6836.7230	0.0580	0.02525
6827.9972	0.9143	0.01216	6832.5768	0.9897	-0.00125	6836.7947	0.0592	0.03187
6828.0684	0.9155	0.01508	6832.6469	0.9909	-0.00493	6837.7800	0.0754	0.04240
6828.1389	0.9167	0.01289	6832.7175	0.9921	-0.00373	6839.2788	0.1001	0.05623
6828.2090	0.9178	0.01174	6832.7881	0.9932	-0.00160	6839.3313	0.1010	0.05782
6828.2796	0.9190	0.01143	6832.8581	0.9944	-0.00331	6839.4048	0.1022	0.05720
6828.3488	0.9201	0.00061	6832.9286	0.9955	-0.00575	6839.4737	0.1033	0.05796
6828.4186	0.9213	-0.01838	6832.9994	0.9967	-0.00193	6839.5459	0.1045	0.05643
6828.4832	0.9283	0.00079	6833.0697	0.9979	0.00270	6839.6122	0.1056	0.05788
6828.5534	0.9294	0.00207	6833.1397	0.9990	-0.00520	6839.6730	0.1066	0.05915
6828.6236	0.9306	0.00721	6833.2104	0.0002	-0.00190	6839.7473	0.1078	0.06494
6829.0543	0.9317	0.00774	6833.2799	0.0013	-0.00538	6839.8159	0.1089	0.06572
6829.1246	0.9329	0.00416	6833.3503	0.0025	0.00320	6839.8878	0.1101	0.06329
6829.1950	0.9341	0.00503	6833.4208	0.0036	0.00924	6839.9577	0.1113	0.05945
6829.2653	0.9352	0.03376	6833.4912	0.0048	-0.00932	6840.0267	0.1124	0.05959
6829.3345	0.9364	0.00897	6833.5628	0.0060	-0.00268	6840.0977	0.1136	0.05971
6829.4058	0.9375	-0.00834	6833.6335	0.0071	0.00216	6840.1957	0.1152	0.05303
6829.4761	0.9387	-0.00641	6833.7033	0.0083	-0.00413	6840.2449	0.1160	0.05419
6829.5472	0.9399	0.00039	6833.7738	0.0094	-0.00021	6840.3181	0.1172	0.05148
6829.6183	0.9410	-0.00026	6833.8445	0.0106	-0.00216	6840.3913	0.1184	0.05015
6829.6879	0.9422	0.00299	6833.9145	0.0118	0.00564	6840.4617	0.1196	0.05459
6829.7591	0.9433	-0.00371	6833.9854	0.0129	0.00338	6840.5291	0.1207	0.05575
6829.8295	0.9445	0.00357	6834.0554	0.0141	0.00818	6840.6001	0.1218	0.06014
6829.8999	0.9457	-0.00823	6834.1259	0.0152	0.00662	6840.6713	0.1230	0.06456
6829.9704	0.9468	0.00077	6834.1963	0.0164	0.01064	6840.7469	0.1243	0.07149
6830.0410	0.9480	-0.00401	6834.2662	0.0176	0.00068	6840.8175	0.1254	0.06395
6830.1112	0.9491	-0.00381	6834.3364	0.0187	-0.00743	6840.8864	0.1266	0.05920
6830.1813	0.9503	-0.00519	6834.4063	0.0199	-0.02639	6840.9562	0.1277	0.05512
6830.2506	0.9514	0.00439	6834.4777	0.0210	-0.00397	6841.0196	0.1287	0.05563
6830.3212	0.9526	-0.00316	6834.5490	0.0222	-0.00527	6841.0959	0.1300	0.05677
6830.3917	0.9538	-0.02045	6834.6203	0.0234	-0.00009	6841.1639	0.1311	0.05555
6830.4620	0.9549	-0.02464	6834.6896	0.0245	-0.00444	6841.2356	0.1323	0.05255
6830.5339	0.9561	-0.00531	6834.7608	0.0257	0.00046	6841.3054	0.1335	0.05054
6830.6042	0.9573	-0.00388	6834.8301	0.0268	-0.00115	6841.3755	0.1346	0.05461
6830.6750	0.9584	-0.00823	6834.9013	0.0280	0.00818	6841.4481	0.1358	0.06025
6830.7454	0.9596	-0.01100	6834.9716	0.0292	0.00543	6841.5153	0.1369	0.05872
6830.8160	0.9607	-0.00541	6835.0420	0.0303	0.01480	6841.5879	0.1381	0.05827
6830.8863	0.9619	-0.00278	6835.1125	0.0315	0.00742	6841.6581	0.1393	0.05432
6830.9569	0.9631	-0.00594	6835.1829	0.0326	0.01615	6841.7287	0.1404	0.04616
6831.0272	0.9642	-0.00492	6835.2525	0.0338	0.02036	6841.8027	0.1416	0.03994
6831.0973	0.9654	-0.01175	6835.3225	0.0349	0.00389	6841.8702	0.1428	0.03817
6831.1679	0.9665	-0.00384	6835.3934	0.0361	-0.00833	6841.9394	0.1439	0.03800
6831.2370	0.9677	0.00352	6835.4646	0.0373	-0.00295	6842.0052	0.1450	0.04399
6831.3072	0.9688	-0.01404	6835.5353	0.0385	0.00110	6842.0801	0.1462	0.04466
6831.3782	0.9700	-0.01552	6835.6059	0.0396	0.01702	6842.1465	0.1473	0.04831
6831.4479	0.9712	-0.03032	6835.6762	0.0408	0.00319	6842.2214	0.1485	0.04867
6831.5203	0.9723	-0.02038	6835.7470	0.0419	0.00620	6842.2912	0.1497	0.04700
6831.5899	0.9735	-0.00677	6835.8174	0.0431	0.01017	6842.3614	0.1508	0.04522
6831.6611	0.9747	-0.01306	6835.8871	0.0442	0.00591	6842.4337	0.1520	0.04290
6831.7315	0.9758	-0.01440	6835.9575	0.0454	0.00987	6842.4995	0.1531	0.03809
6831.8017	0.9770	-0.00947	6836.0280	0.0466	0.02004	6842.5727	0.1543	0.03615
6831.8720	0.9781	-0.00791	6836.0988	0.0477	0.01839	6842.6434	0.1555	0.03611
6831.9429	0.9793	-0.00785	6836.1692	0.0489	0.01539	6842.7160	0.1567	0.03792
6832.0128	0.9805	0.00241	6836.2383	0.0500	0.02371	6842.7858	0.1578	0.03724
6832.0838	0.9816	-0.00308	6836.3089	0.0512	0.01848	6842.8556	0.1590	0.03884

**Table A6** – *continued* Orbital light curve from *MOST*

JD - 2,450,000	Phase	$\Delta m$ (mag)	JD - 2,450,000	Phase	$\Delta m$ (mag)	JD - 2,450,000	Phase	$\Delta m$ (mag)
6842.9280	0.1602	0.04261	6853.4190	0.3329	-0.04118	6857.6448	0.4025	-0.04528
6842.9974	0.1613	0.04537	6853.4886	0.3341	-0.04578	6857.7144	0.4036	-0.04485
6843.0648	0.1624	0.04647	6853.5588	0.3352	-0.04650	6857.7631	0.4044	-0.04807
6843.1376	0.1636	0.04730	6853.6298	0.3364	-0.04809	6859.3455	0.4305	-0.03419
6843.2088	0.1648	0.04153	6853.7017	0.3376	-0.04638	6859.4002	0.4314	-0.02815
6843.2718	0.1658	0.04231	6853.7698	0.3387	-0.04539	6859.4605	0.4324	-0.02368
6843.3470	0.1671	0.03855	6853.8429	0.3399	-0.04695	6860.2651	0.4456	-0.02287
6843.4217	0.1683	0.03433	6853.9112	0.3410	-0.04553	6860.3200	0.4465	-0.03143
6843.4888	0.1694	0.04293	6853.9821	0.3422	-0.04005	6860.3902	0.4477	-0.02512
6843.5608	0.1706	0.04146	6854.0531	0.3433	-0.03356	6860.4603	0.4488	-0.03027
6843.6319	0.1718	0.04570	6854.1245	0.3445	-0.03652	6860.5307	0.4500	-0.02811
6843.6992	0.1729	0.05073	6854.1916	0.3456	-0.04175	6860.6021	0.4512	-0.03394
6843.7721	0.1741	0.04827	6854.2627	0.3468	-0.04285	6860.6676	0.4523	-0.01720
6843.8430	0.1752	0.04627	6854.3327	0.3479	-0.04590	6860.7458	0.4535	-0.02614
6843.9139	0.1764	0.04000	6854.4037	0.3491	-0.04148	6860.8145	0.4547	-0.02307
6843.9826	0.1775	0.03762	6854.4739	0.3503	-0.03919	6860.8823	0.4558	-0.02226
6844.0540	0.1787	0.03054	6854.5450	0.3514	-0.03659	6860.9521	0.4569	-0.02177
6844.1216	0.1798	0.02976	6854.6157	0.3526	-0.03042	6861.0251	0.4581	-0.02052
6844.1918	0.1810	0.02832	6854.6904	0.3538	-0.02877	6861.0917	0.4592	-0.01903
6844.2643	0.1822	0.02399	6854.7566	0.3549	-0.03074	6861.1581	0.4603	-0.01971
6844.3347	0.1833	0.02292	6854.8302	0.3561	-0.03000	6861.2353	0.4616	-0.02122
6844.4031	0.1845	0.02804	6854.8973	0.3572	-0.03682	6861.3063	0.4628	-0.02858
6844.4734	0.1856	0.02990	6854.9685	0.3584	-0.04125	6861.3756	0.4639	-0.02976
6844.5468	0.1868	0.03491	6855.0402	0.3596	-0.04338	6861.4458	0.4651	-0.02878
6844.6183	0.1880	0.03654	6855.1073	0.3607	-0.04329	6861.5165	0.4662	-0.02567
6844.6873	0.1891	0.03621	6855.1778	0.3619	-0.04182	6861.5898	0.4674	-0.02274
6844.7518	0.1902	0.03674	6855.2470	0.3630	-0.04142	6861.6597	0.4686	-0.02256
6844.8255	0.1914	0.03653	6855.3203	0.3642	-0.03787	6861.7303	0.4697	-0.01747
6844.8770	0.1923	0.04554	6855.3893	0.3653	-0.03743	6861.7984	0.4709	-0.02051
6848.0850	0.2451	0.00048	6855.4637	0.3666	-0.03473	6861.8696	0.4720	-0.01779
6848.1374	0.2459	0.00382	6855.5323	0.3677	-0.03460	6861.9403	0.4732	-0.00595
6848.2073	0.2471	0.00014	6855.6028	0.3689	-0.03850	6862.0069	0.4743	-0.01727
6848.2781	0.2483	-0.00217	6855.6730	0.3700	-0.03758	6862.0786	0.4755	-0.01329
6848.3492	0.2494	-0.00336	6855.7461	0.3712	-0.04064	6862.1474	0.4766	-0.00540
6848.4193	0.2506	0.00030	6855.8160	0.3724	-0.03970	6862.2134	0.4777	0.00300
6848.4888	0.2517	-0.00276	6855.8822	0.3735	-0.04297	6862.2908	0.4790	0.01150
6848.5547	0.2528	-0.00657	6855.9546	0.3747	-0.04321	6862.3347	0.4797	-0.02169
6848.6287	0.2540	-0.01074	6856.0262	0.3758	-0.04070	6862.4513	0.4816	-0.02406
6848.7024	0.2552	-0.01152	6856.0900	0.3769	-0.03539	6862.5026	0.4825	-0.01163
6848.7710	0.2564	-0.00968	6856.1627	0.3781	-0.02474	6862.5726	0.4836	-0.00850
6848.8455	0.2576	-0.01502	6856.2346	0.3793	-0.02727	6862.6445	0.4848	-0.01311
6848.9116	0.2587	-0.01942	6856.3061	0.3804	-0.02991	6862.7123	0.4859	-0.01690
6848.9825	0.2599	-0.01607	6856.3751	0.3816	-0.02864	6862.7812	0.4871	-0.01334
6849.0499	0.2610	-0.01132	6856.4481	0.3828	-0.03227	6862.8536	0.4882	-0.01190
6849.1208	0.2621	-0.00555	6856.5183	0.3839	-0.03410	6862.9214	0.4894	-0.02091
6849.1943	0.2633	-0.00257	6856.5871	0.3851	-0.03461	6862.9938	0.4906	-0.02148
6849.2659	0.2645	-0.00270	6856.6608	0.3863	-0.03427	6863.0655	0.4917	-0.02445
6849.3328	0.2656	-0.00615	6856.7267	0.3874	-0.03557	6863.1326	0.4928	-0.02499
6849.4054	0.2668	-0.00636	6856.8022	0.3886	-0.03091	6863.1995	0.4939	-0.01970
6849.4553	0.2676	-0.01642	6856.8738	0.3898	-0.03651	6863.2755	0.4952	-0.01856
6852.7259	0.3215	-0.04401	6856.9380	0.3908	-0.03627	6863.3467	0.4964	-0.01178
6852.7890	0.3225	-0.04841	6857.0092	0.3920	-0.04155	6863.4177	0.4975	-0.01084
6852.8552	0.3236	-0.05120	6857.0819	0.3932	-0.03586	6863.4821	0.4986	-0.01188
6852.9265	0.3248	-0.04577	6857.1494	0.3943	-0.03580	6863.5579	0.4998	-0.01291
6852.9962	0.3259	-0.04957	6857.2187	0.3955	-0.04584	6863.6281	0.5010	-0.02005
6853.0633	0.3270	-0.03773	6857.2905	0.3966	-0.04543	6863.6998	0.5022	-0.02510
6853.1344	0.3282	-0.03876	6857.3570	0.3977	-0.04551	6863.7691	0.5033	-0.02042
6853.2075	0.3294	-0.03760	6857.4310	0.3990	-0.04588	6863.8413	0.5045	-0.01763
6853.2736	0.3305	-0.03834	6857.5018	0.4001	-0.05396	6863.9123	0.5057	-0.01640
6853.3438	0.3317	-0.04217	6857.5726	0.4013	-0.04652	6863.9811	0.5068	-0.02477

**Table A6** – *continued* Orbital light curve from *MOST*

JD - 2,450,000	Phase	$\Delta m$ (mag)	JD - 2,450,000	Phase	$\Delta m$ (mag)	JD - 2,450,000	Phase	$\Delta m$ (mag)
6864.0514	0.5080	-0.02341	6864.8261	0.5207	-0.01528	6868.8420	0.5868	-0.00514
6864.1220	0.5091	-0.02047	6864.8986	0.5219	-0.01304	6868.9894	0.5893	0.00029
6864.1923	0.5103	-0.01894	6864.9685	0.5231	-0.01478	6869.0531	0.5903	-0.00131
6864.2616	0.5114	-0.01585	6865.0374	0.5242	-0.01522	6869.1235	0.5915	0.00349
6864.3325	0.5126	-0.01442	6865.1080	0.5254	-0.01815	6869.1928	0.5926	0.00137
6864.4097	0.5139	-0.01857	6865.1787	0.5265	-0.02022	6869.2640	0.5938	0.00109
6864.4738	0.5149	-0.02090	6865.2513	0.5277	-0.02008	6869.3326	0.5949	0.00496
6864.5445	0.5161	-0.01994	6865.3190	0.5288	-0.02510	6869.4040	0.5961	0.00343
6864.6154	0.5173	-0.02043	6865.3875	0.5300	-0.02227	6869.4738	0.5972	-0.00084
6864.6861	0.5184	-0.02079	6865.4597	0.5312	-0.02362	6869.5458	0.5984	0.00061
6864.7562	0.5196	-0.01275	6868.7799	0.5858	-0.00274	6869.6164	0.5996	0.00379

**Table A7.** Pulsational light curve from *MOST*

JD - 2,450,000	$\Delta m$ (mag)	JD - 2,450,000	$\Delta m$ (mag)	JD - 2,450,000	$\Delta m$ (mag)	JD - 2,450,000	$\Delta m$ (mag)	JD - 2,450,000	$\Delta m$ (mag)
6827.5753	0.00733	6833.7763	0.00080	6841.0668	-0.00696	6848.5935	0.00229	6856.1150	0.00565
6827.6459	0.00627	6833.8471	-0.00255	6841.1386	-0.00599	6848.6641	0.00016	6856.1864	0.00559
6827.7164	0.00475	6833.9178	0.00068	6841.2086	-0.00566	6848.7312	-0.00070	6856.2571	0.00528
6827.7871	0.00264	6833.9879	-0.00031	6841.2815	-0.00493	6848.8045	-0.00104	6856.3371	0.00376
6827.8579	-0.00107	6834.0591	0.00398	6841.3531	0.00181	6848.8771	-0.01215	6856.4108	-0.00559
6827.9291	-0.00801	6834.1295	-0.00384	6841.4261	0.00420	6848.9516	-0.00793	6856.4819	-0.01185
6827.9993	-0.00739	6834.1999	-0.00202	6841.5038	0.00727	6849.0253	-0.00299	6856.5496	-0.00970
6828.0702	-0.00465	6834.2705	-0.00280	6841.5779	0.00556	6849.0968	0.00220	6856.6229	-0.01001
6828.1407	0.00171	6834.5490	0.00505	6841.6504	0.00285	6849.1676	0.00657	6856.6909	-0.00903
6828.2112	0.00217	6834.6200	0.00799	6841.7268	-0.00124	6849.2372	0.00487	6856.7572	-0.00325
6828.2836	-0.00236	6834.6914	0.00534	6841.7994	-0.00075	6849.3129	0.00545	6856.8293	0.00050
6828.3547	-0.00340	6834.7619	0.00217	6841.8860	-0.00486	6849.3794	-0.00628	6856.9030	0.00763
6828.4261	0.00407	6834.8326	-0.00218	6841.9566	-0.00275	6849.4509	-0.01807	6856.9746	0.00772
6828.4975	0.00640	6834.9027	0.00004	6842.0321	0.00116	6852.7149	-0.00531	6857.0488	0.00771
6829.0000	0.00702	6834.9738	-0.00553	6842.0975	0.00577	6852.7954	-0.00292	6857.1181	0.00316
6829.0614	0.00335	6835.0446	-0.00427	6842.1701	0.00480	6852.8645	-0.00280	6857.1934	0.00564
6829.1228	-0.00106	6835.1150	-0.00598	6842.2395	0.00813	6852.9366	0.00874	6857.2647	-0.00077
6829.1842	-0.00729	6835.1855	0.00346	6842.3314	0.00144	6853.0177	0.01266	6857.3374	-0.00140
6829.2456	-0.00695	6835.2560	0.00396	6842.4032	-0.00060	6853.0853	0.01653	6857.4078	-0.00372
6829.3070	-0.00373	6835.3265	-0.00367	6842.4739	-0.01005	6853.1568	0.01550	6857.4782	-0.00556
6829.3684	-0.00247	6835.3970	-0.00430	6842.5445	-0.01488	6853.2297	0.00970	6857.5486	-0.00543
6829.4298	0.00404	6835.4675	-0.00640	6842.6167	-0.01600	6853.3015	0.00384	6857.6190	-0.00103
6829.4912	0.00211	6835.5380	-0.00327	6842.6896	-0.01083	6853.3739	-0.00157	6857.6908	0.00393
6829.5526	0.00494	6835.6085	0.00135	6842.7620	-0.00289	6853.4467	-0.00755	6857.7626	0.00769
6829.6140	0.00493	6835.6790	0.00027	6842.8343	0.00348	6853.5191	-0.01434	6857.8344	0.00238
6829.6754	0.00157	6835.7495	0.00556	6842.9067	0.01316	6853.5915	-0.01420	6857.9062	0.00381
6829.7368	-0.00087	6835.8200	0.00515	6843.0161	0.01633	6853.6639	-0.00750	6857.9780	-0.00244
6829.7982	-0.00246	6835.8905	0.01547	6843.0884	0.01684	6853.7363	-0.00300	6858.0498	0.00304
6829.8596	0.00514	6835.9610	0.00518	6843.1608	0.00941	6853.8087	0.00057	6858.1216	0.00282
6829.9210	0.00367	6836.0315	0.00325	6843.2332	0.00194	6853.8811	0.00484	6858.1934	-0.00648
6829.9824	0.00334	6836.1020	-0.00476	6843.3056	-0.00004	6853.9535	0.01128	6858.2652	-0.00862
6830.0438	-0.00072	6836.1725	-0.00554	6843.3780	-0.00756	6854.0259	0.01047	6858.3370	-0.00929
6830.1052	-0.00205	6836.2430	-0.00122	6843.4504	-0.00826	6854.0983	0.00465	6858.4088	-0.00932
6830.1666	-0.00148	6836.3135	0.00244	6843.5228	-0.00867	6854.1707	0.00007	6858.4806	-0.00525
6830.2280	-0.00154	6836.3840	0.00625	6843.5952	-0.00520	6854.2431	-0.00085	6858.5524	0.00003
6830.2894	-0.00507	6836.4545	0.00025	6843.6676	0.00218	6854.3155	-0.00360	6858.6242	0.00329
6830.3508	0.00162	6836.5250	0.01004	6843.7400	0.00525	6854.3879	0.00308	6858.6960	0.00185
6830.4122	0.00348	6836.5955	0.00679	6843.8124	0.00851	6854.4603	0.00127	6858.7678	0.00167
6830.4736	0.01217	6836.6660	0.00014	6843.8848	0.00054	6854.5327	0.00242	6858.8396	0.00090
6830.5350	0.00517	6836.7365	-0.00521	6843.9572	0.00197	6854.6051	0.00685	6858.9114	0.00067
6830.5964	0.00076	6836.8070	-0.00929	6844.0296	0.00109	6854.6775	0.00531	6858.9832	-0.00161
6830.6578	-0.00258	6836.8775	-0.00389	6844.1020	-0.00240	6854.7500	0.00886	6859.0550	0.00053
6830.7192	-0.00557	6836.9480	0.00100	6844.1744	-0.00582	6854.8224	0.00414	6859.1268	0.00053
6830.7806	-0.00854	6837.0185	0.01277	6844.2468	-0.00924	6854.8948	-0.00657	6859.1986	0.00665
6830.8420	-0.00634	6837.0890	0.01235	6844.3192	-0.00627	6854.9672	-0.00423	6859.2704	0.00338
6830.9034	-0.00227	6837.1595	0.01620	6844.3916	-0.00090	6855.0396	-0.01034	6859.3422	0.00524
6830.9648	-0.00393	6837.2300	0.02147	6844.4640	0.00152	6855.1120	-0.01359	6859.4140	0.00380
6831.0262	0.00273	6837.3005	0.01248	6844.5364	0.00469	6855.1844	-0.00659	6859.4858	-0.00078
6831.0876	-0.00501	6837.3710	-0.00033	6844.6088	0.00557	6855.2568	-0.00122	6859.5576	-0.00258
6831.1490	-0.00441	6837.4415	0.00270	6844.6812	0.00730	6855.3292	-0.00089	6859.6294	-0.00572
6831.2104	-0.00375	6837.5120	-0.00265	6844.7536	0.00257	6855.4016	0.00487	6859.7012	-0.02406
6831.2718	-0.00007	6837.5825	-0.00267	6844.8260	0.00081	6855.4740	0.00637	6859.7730	-0.01701
6831.3332	0.00479	6837.6530	-0.00251	6844.8984	-0.00611	6855.5464	0.00208	6859.8448	-0.01179
6831.3946	0.01076	6837.7235	0.00089	6844.9708	-0.01090	6855.6188	-0.00086	6859.9166	-0.00447
6831.4560	0.00355	6837.7940	0.00697	6845.0432	-0.00641	6855.6912	-0.00502	6860.0000	0.00000
6831.5174	0.00385	6837.8645	0.00911	6845.1156	-0.00618	6855.7636	0.00182	6860.0718	0.00333
6831.5788	-0.00121	6837.9350	0.01431	6845.1880	0.00378	6855.8360	0.00233	6860.1436	0.00937
6831.6402	-0.00313	6838.0055	0.00026	6845.2604	0.00854	6855.9084	-0.00240	6860.2154	-0.01004
6831.7016	0.00321	6838.0760	-0.00365	6845.3328	0.01032	6855.9808	0.00021	6860.2872	-0.00697
6831.7630	0.00287	6838.1465	-0.00386	6845.4052	0.00668	6856.0532	0.00068	6860.3590	-0.00082



Table A7 – continued Pulsational light curve from MOST

JD - 2,450,000	$\Delta m$ (mag)	JD - 2,450,000	$\Delta m$ (mag)	JD - 2,450,000	$\Delta m$ (mag)	JD - 2,450,000	$\Delta m$ (mag)	JD - 2,450,000	$\Delta m$ (mag)
6863.0706	0.00115	6870.0491	0.01288	6873.7126	-0.00677	6877.7261	0.00398	6881.5280	0.00519
6863.1424	0.00144	6870.1210	0.00844	6873.7838	0.00184	6877.7995	0.00754	6881.5981	0.00608
6863.2119	0.00268	6870.1926	0.00392	6873.8571	-0.00036	6877.8684	0.00038	6881.6716	0.00596
6863.2800	0.00096	6870.2622	0.00049	6873.9283	0.00287	6877.9398	-0.00709	6881.7418	0.00359
6863.3487	-0.00085	6870.3854	-0.00526	6874.0623	0.00617	6878.0116	-0.00550	6881.8836	-0.00381
6863.4229	0.00134	6870.4594	-0.00356	6874.1345	0.00229	6878.0820	-0.00601	6881.9544	-0.00612
6863.4945	-0.00140	6870.5351	-0.00558	6874.2077	-0.00211	6878.1538	-0.00415	6882.0261	-0.00315
6863.5688	-0.00283	6870.6039	-0.00509	6874.3398	-0.00018	6878.2248	-0.00077	6882.0971	-0.00433
6863.6381	-0.00315	6870.7437	0.00123	6874.4803	-0.00064	6878.3539	0.00324	6882.1680	-0.00181
6863.7089	-0.00449	6870.8201	0.00390	6874.5578	0.00118	6878.4273	0.00431	6882.2406	0.00159
6863.7811	0.00278	6870.8882	0.00581	6874.6285	0.00477	6878.4994	0.00827	6882.3702	0.00158
6863.8473	0.00608	6870.9615	0.00036	6874.6987	0.00463	6878.5739	0.00705	6882.4418	0.00269
6863.9221	0.00581	6871.0324	-0.00010	6874.7720	0.00288	6878.6448	0.00539	6882.5183	0.00185
6863.9926	0.00099	6871.1037	-0.00104	6874.8405	0.00386	6878.7147	0.00166	6882.7319	0.00027
6864.0633	0.00174	6871.1747	-0.00189	6874.9124	-0.00497	6878.7873	-0.00109	6882.8683	-0.00192
6864.1334	-0.00352	6871.2453	-0.00177	6874.9829	-0.00405	6878.8588	-0.00057	6882.9387	-0.00091
6864.2041	-0.00061	6871.3116	-0.00129	6875.0527	-0.00623	6878.9296	-0.00145	6883.0110	0.00159
6864.2697	-0.00371	6871.3820	0.00182	6875.1266	-0.00733	6878.9995	-0.00534	6883.0813	0.00144
6864.4058	-0.00288	6871.4532	0.00494	6875.1971	-0.00318	6879.0706	0.00181	6883.1515	0.00242
6864.4808	0.00157	6871.5283	0.00676	6875.3264	0.00173	6879.1417	-0.00031	6883.2239	0.00110
6864.5546	0.00161	6871.6011	0.00782	6875.3981	0.00262	6879.2709	0.00163	6883.3541	0.00053
6864.6273	0.00324	6871.6711	0.00593	6875.4699	0.00272	6879.3414	0.00212	6883.4273	-0.00392
6864.6973	0.00036	6871.7416	0.00096	6875.5433	0.00490	6879.4125	0.00155	6883.4989	-0.00664
6864.7676	0.00066	6871.8139	0.00038	6875.6157	0.00125	6879.4843	-0.00358	6883.5767	-0.00564
6864.8394	0.00152	6871.8843	-0.00202	6875.7549	-0.00044	6879.5587	-0.00395	6883.6489	-0.00184
6864.9108	-0.00378	6871.9555	-0.00311	6875.8224	-0.00019	6879.6319	-0.00138	6883.7206	-0.00107
6864.9823	-0.00312	6872.0262	-0.00488	6875.8957	-0.00109	6879.7038	-0.00157	6883.7911	0.00144
6865.0526	-0.00406	6872.0990	-0.00388	6875.9656	0.00003	6879.7740	-0.00025	6883.9271	0.00721
6865.1241	-0.00080	6872.1693	0.00232	6876.0364	0.00230	6879.8437	-0.00120	6884.0028	0.00509
6865.1948	-0.00086	6872.2885	0.00315	6876.1075	0.00384	6879.9166	0.00305	6884.1373	0.00019
6865.2653	0.00047	6872.3570	0.00179	6876.1802	0.00127	6879.9870	0.00503	6884.2097	-0.00112
6865.3835	0.00258	6872.4298	0.00205	6876.3115	-0.00082	6880.1214	0.00837	6884.3419	-0.00008
6865.4544	0.00413	6872.5083	-0.00097	6876.3813	-0.00267	6880.1927	0.00353	6884.4125	0.00185
6868.7794	-0.00031	6872.5841	-0.00123	6876.4543	-0.00711	6880.2588	0.00112	6884.4841	-0.00080
6868.8512	-0.00206	6872.6543	-0.00390	6876.5265	-0.00697	6880.3292	-0.00652	6884.5629	0.00767
6868.9877	0.00180	6872.7254	-0.00454	6876.6017	-0.00727	6880.3996	-0.00576	6884.6335	0.00770
6869.0585	0.00019	6872.7981	-0.00083	6876.6705	-0.00706	6880.4705	-0.00580	6884.7057	0.00689
6869.1325	0.00411	6872.8689	0.00025	6876.7422	-0.00196	6880.5453	-0.00545	6884.7759	0.00727
6869.2027	0.00472	6872.9405	0.00149	6876.8155	0.00070	6880.6173	-0.00278	6884.8473	-0.00179
6869.2686	0.00893	6873.0115	0.00351	6876.8846	0.00901	6880.6868	-0.00145	6884.9189	0.00120
6869.3385	0.00271	6873.0828	0.00772	6876.9553	0.01221	6880.7588	0.00431	6884.9894	-0.00493
6869.4092	-0.00031	6873.2164	0.00183	6877.0278	0.00718	6880.8308	0.00551	6885.1231	0.00006
6869.4807	-0.00113	6873.2834	0.00020	6877.1632	-0.00074	6880.9015	0.00287		
6869.5536	-0.00227	6873.3553	-0.01183	6877.2339	-0.00111	6880.9732	0.00176		
6869.6250	-0.00538	6873.4251	-0.01208	6877.3685	-0.00219	6881.0440	0.00207		
6869.6939	-0.00387	6873.4971	-0.01316	6877.5114	-0.00116	6881.1770	-0.00255		
6869.8329	0.00582	6873.5714	-0.01411	6877.5857	0.00066	6881.2480	-0.00396		
6869.9801	0.01055	6873.6427	-0.00979	6877.6559	0.00481	6881.3137	0.00184		

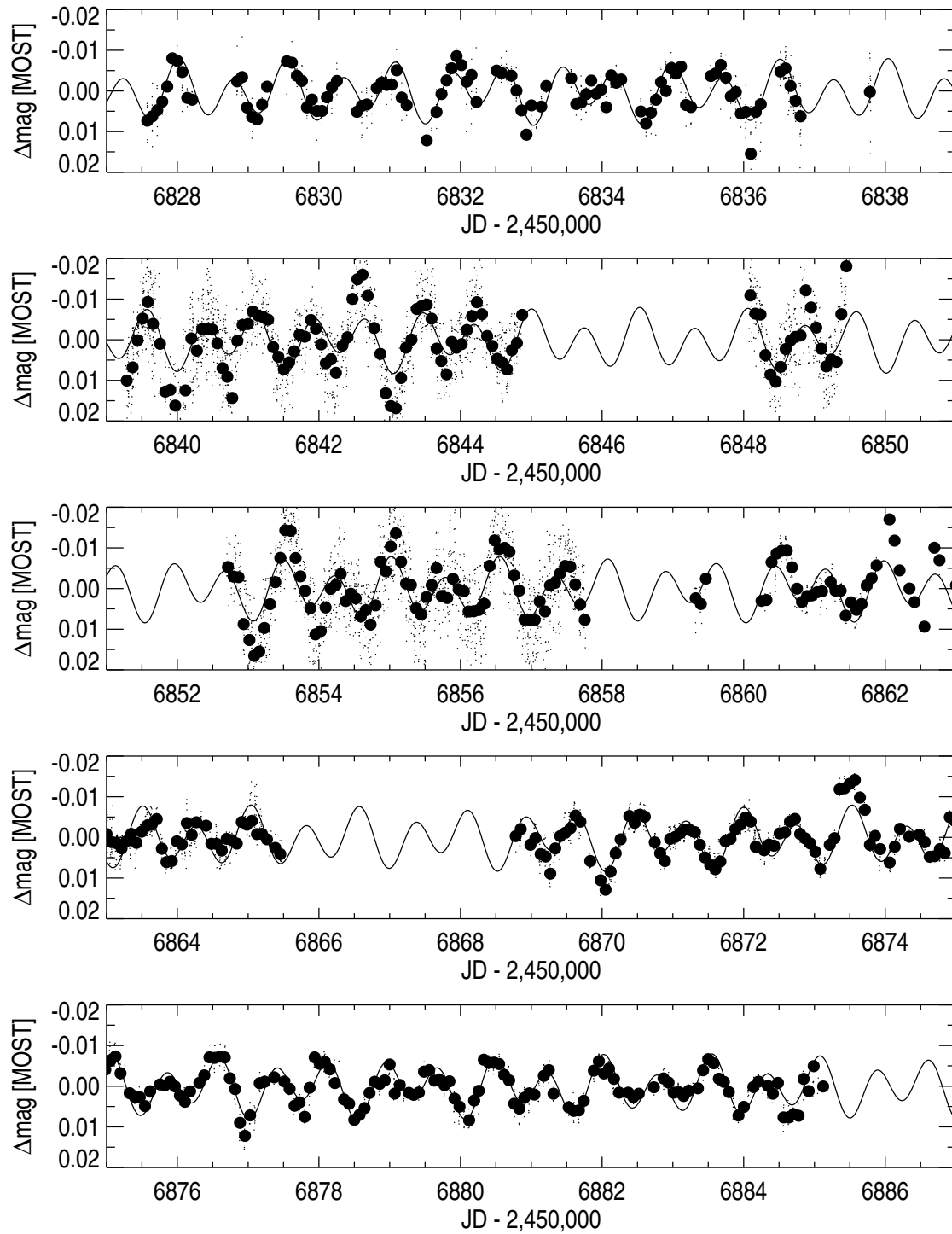


**Figure A2.** The entire de-trended *MOST* light curve, with our two frequency fit overplotted. The detrending has removed the orbitally modulated variation, and only pulsational behaviour remains. Small points represent individual measurements, with the large points representing the orbital means.